Improvement in Electrochemical Properties of NASICON-type Electrode Active Materials for Li-ion Battery

奇, 龍鎬

https://doi.org/10.15017/1785429

出版情報：九州大学, 2016, 博士（工学）, 課程博士
バージョン：
権利関係：全文ファイル公表済

Improvement in Electrochemical Properties of NASICON-type Electrode Active Materials for Li-ion Battery

Supervisor: Prof. Shigeto Okada

YONGHO KEE

Interdisciplinary Graduate School of Engineering Sciences

Kyushu University

CONTENTS

CHAPTER 1

Introduction

1.1 Secondary Batteries

In recent years, Li-ion secondary batteries have been widely investigated as future energy storage system. Several advantages make current Li-ion batteries attractive because:

· lithium shows highly ionizable operating voltage of -3.04 V for Li^+/Li vs. SHE (This value provides high energy density considering E^o for Pb^{2+}/Pb is only -0.126 V vs. SHE in lead-acid battery),

· Li-ion secondary battery does not show memory effect and detrimental self-discharging, while conventional batteries largely suffer from continuous capacity loss,

· Li-based materials require less costs for disposal thus environmentally benign compare to lead-acid battery.

The general cell reactions of several rechargeable batteries are listed in **Table 1-1**. As seen from **Table 1-1**, Li-ion batteries clearly show the highest energy density. Every Li-ion battery consists of four components: cathode, anode, electrolyte, and separator. During discharging process, Li-ions migrate to cathode side, electrons move through the wire and Li-ions and electrons revert back to their original positions during the charging process.

Table 1-1. Main types of secondary batteries with reaction formula, discharge potentials and energy densities.

Type	**Reaction formula**	**Discharge potential [V vs. Li]**	**Energy density [Wh/l]**
NiFe	$2NiOOH + 2H_2O + 2e^- \rightarrow 2Ni(OH)_2 + 2OH^-$ $M + 2OH^- \rightarrow M(OH)_2 + 2e^-$ (M = Fe, Cd, or Zn)	1.2 V	~ 30
NiCd		1.2 V	~ 150
NiZn		1.65 V	~ 280
Lead-acid	$Pb + HSO_4^- \rightarrow PbSO_4 + H^+ + 2e^-$ $PbO_2 + HSO_4^- + 3H^+ + 2e^- \rightarrow PbSO_4 + 2H_2O$	2.0 V	~ 110
NiMH	$H_2O + M + e^- \rightarrow OH^- + MH$ $Ni(OH)_2 + OH^- \rightarrow NiO(OH) + H_2O + e^-$ (M = intermetallic compound)	1.2 V	~ 300
Li-ion	$LiCoO_2 \rightarrow Li_{1-x}CoO_2 + xLi^+ + xe^-$ $xLi^+ + xe^- + xC_6 \rightarrow xLiC_6$	3.7 V	~ 620

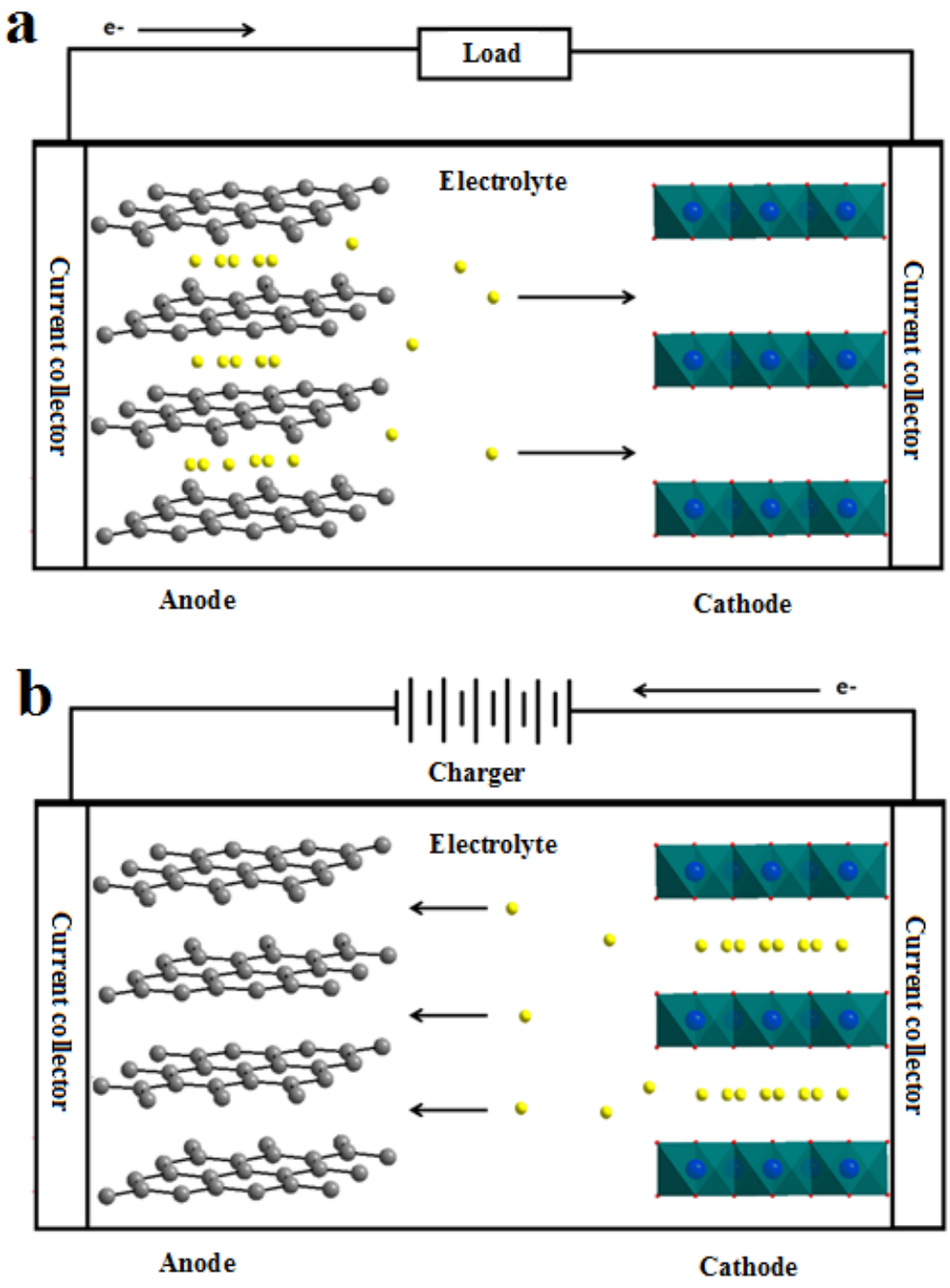

Fig. 1-1 Sketch of a typical lithium-ion battery.

A sketch of a typical lithium-ion battery is shown in **Fig. 1-1**. As electrode materials should enable (de)intercalation of Li-ions during cell reactions, various electrode materials with multidimensional channels for Li-ion to pass through have been widely investigated. Materials having representative structures are: layered $LiCoO_2$, cubic $LiMn_2O_4$ structure, $Li_3V_2(PO_4)_3$, and olivine $LiFePO_4$ as all shown in **Fig. 1-2**.

As electrode materials should enable (de)intercalation of Li-ions during cell reactions, various electrode materials with multidimensional channels for Li-ion to pass through have been widely investigated. Materials having representative structures are: layered rocksalt-type $LiCoO_2$, spinel-type $LiMn_2O_4$, olivine-type $LiFePO_4$, and NASICON-type $Li_3V_2(PO_4)_3$ as all shown in **Fig. 1-2**.

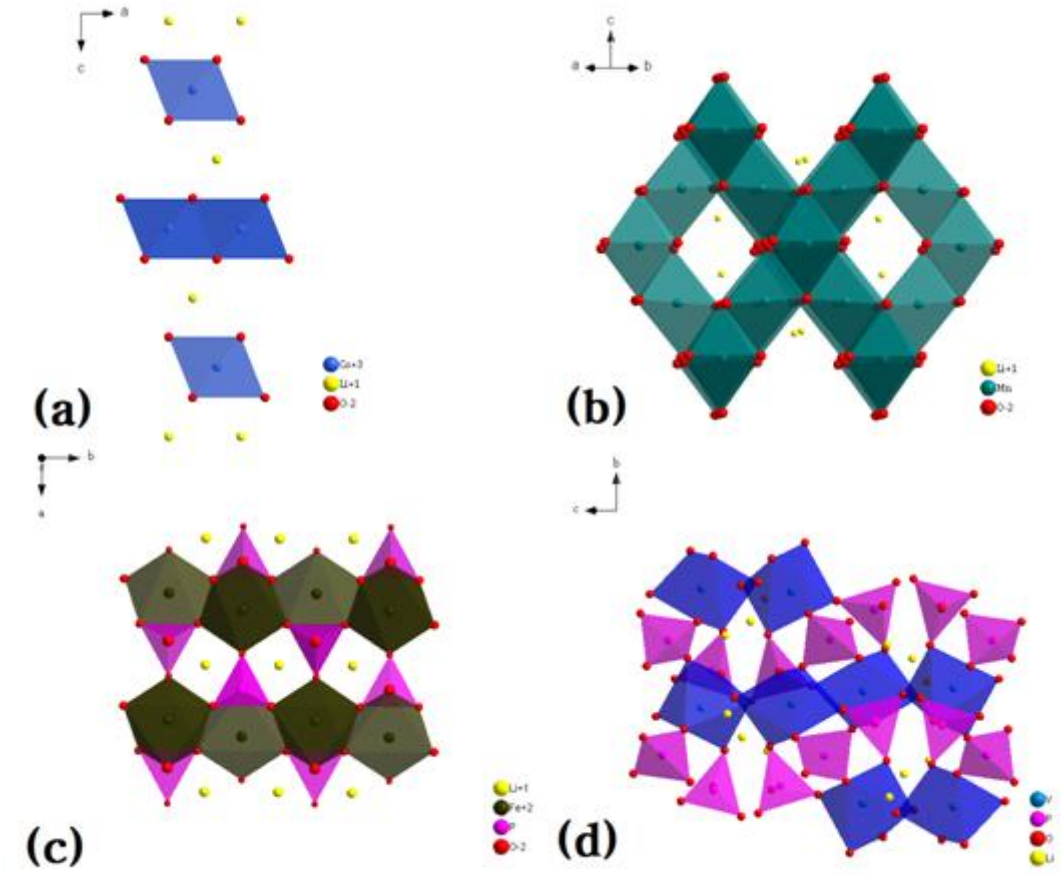

Fig. 1-2 The main groups of cathode materials for lithium-ion batteries: (a) Layered rocksalt-type $LiCoO_2$; Li^+ can move in two dimensional van der Waals gap between the oxygen sheets (b) Spinel-type $LiMn_2O_4$; Li^+ can move along all three crystallographic axes a, b, and c (c) Olivine-type $LiFePO_4$; Li^+ diffusion is restricted to one dimensional tunnels along b-axis (d) NASICON-type $Li_3V_2(PO_4)_3$; Li^+ diffusion follows complex bent pathways.

1.2 Introduction to NASICON-type materials

Clearly, NASICON structures are the most complex compound with many possible variations. Although all these compounds can be utilized as Li^+ hosts with satisfactory reversibility, high production cost, limited resource reserves, and thermal instability especially of the layered materials in their charged state still remain major limitations for large scale applications. Among various choices of electrode materials, NASICON-type (NAtrium SuperIonic CONductor) materials have shown promising electrochemical properties as electrode candidates. First, NASICON-type framework could utilize strong inductive effect from the polyanion group XO_4 (X = P, S, Si, Mo, etc), which makes them possible to tune redox potential of the transition metal couple $M^{(n+1)+}/M^{n+}$. This feature allows doping various transition metals in the octahedral MO_6 (M = Sc, V, Fe, Al, Ti, Nb, etc) coordination. Changing the transition metal, M, results in distortion of the octahedra and there are many NASICON compounds with various number of Li-ion sites.

Figure 1-3 shows NASICON-framework, which consists of XO_4 tetrahedra linking together with MO_6 octahedra making 3-D channels for Li-ion to reside in. There is a fairly standard way to build the NASICON structures. It is commonly assumed that within one and the same anioinic framework $Li_xMO_6XO_4$, Li ions tend to reside into 6-fold coordinated M1 sites.

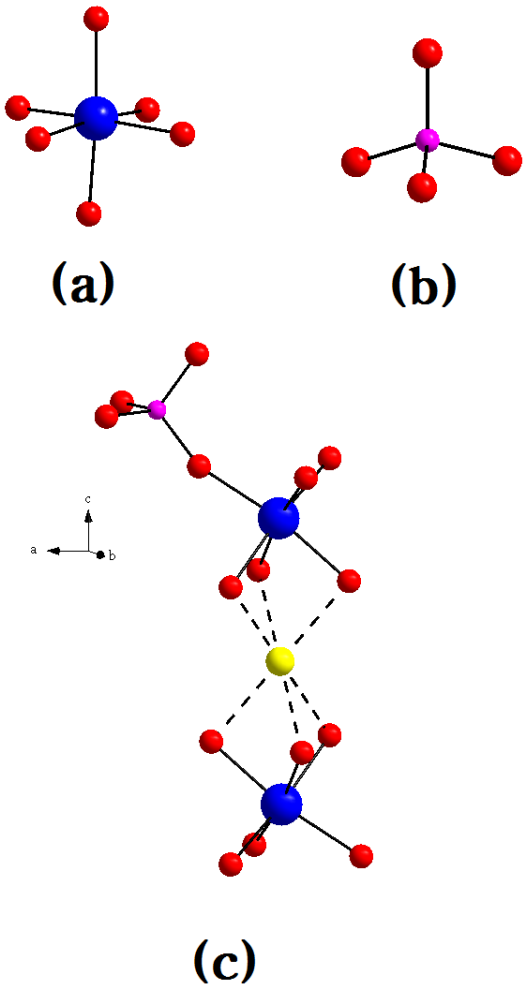

Fig. 1-3 Schematic view of MO_6 octahedra (a), XO_4 tetrahedra (b), and Li-ion in M1 site (c).

When the 6-fold coordinated M1 sites become completely occupied, further increase of the Li content in $Li_xMO_6XO_4$ results in gradual occupation of the 8-fold coordinated M2 sites. It is often assumed that the ionic flows between these two sites account for the ionic conduction and Li^+ diffusion in the crystalline framework of the NASICON-type materials. As a rule of thumb, it should be assumed that the prototype structure of the NASICON-type materials has rhombohedral symmetry. However, this is extremely feature-rich structure from crystallographic viewpoint. For example, depending on the type of the transition metal M and lithium content, x, $Li_xMO_6XO_4$ could have a variety of possible structural modifications. Several possible NASICON structural motifs, which cover four different structures in the NASICON family of solid states, are shown in **Fig. 1-4**. Only a few of these structures might be interesting as possible active materials for lithium-ion batteries. This is because various conditions should be simultaneously satisfied:

1. The structure should contain transition metal in appropriate oxidation state

2. There should exist appropriate diffusion channels

3. There should be minimal or low energy phase transition between the lithiated and de-lithiated states

4. It is desirable that the phases have low band gaps, i.e. they are comparatively good current conductors

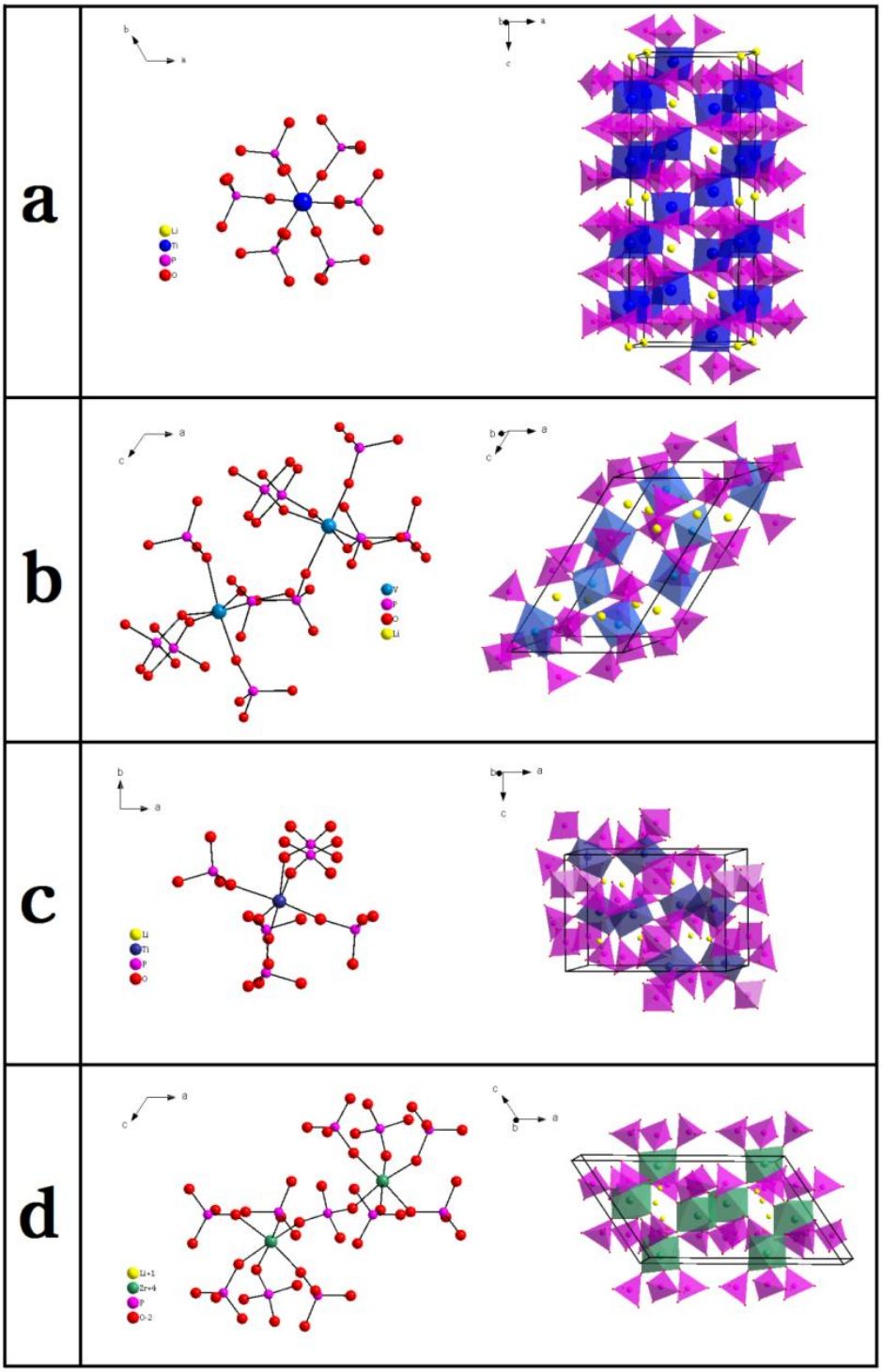

Fig. 1-4 Atomic coordination around central metal and 3-D linking modes of rhombohedral phase (a), monoclinic phase (b), orthorhombic phase (c), and triclinic phase (ICSD #89456, d).

In most of the cases one or more of these conditions are not met and the corresponding phases could not be used as active battery materials. Among these systems, monoclinic $Li_3V_2(PO_4)_3$ works in appropriate potential range and has decent capacity, which is known as anti-NASICON phase, which is also known as β-$Fe_2(SO_4)_3$-type or α-phase. The major differences between these structures are distribution of Li-sites and distortion of MO_6 octahedra induced by its linking with PO_4 tetrahedra [2–4].

So far, various polymorphs with monoclinic $Li_3V_2(PO_4)_3$ structure have been reported. Also known are the primitive rhombohedral phase adopted by $LiTi_2(PO_4)_3$, the orthorhombic phase (Superionic phase), and the triclinic phase.

These phases could be typically induced by the following two ways: i) upon heating; ii) by doping aliovalent cation on metal sites. **Figure 1-5** shows the diversity of structures which belong to the NASICON family of compounds and the possible transition pathways between these phases. **Figure 1-5** clearly shows the rich structural diversity and complex transition pathways in the NASICON family of solid states. It should be emphasized that this figure may represent only a fraction of the real complexity, i.e. it does not include all possibilities, but only a fraction of the complete exploration space.

In a relatively short work (i.e. this PhD thesis), I cannot cover all structural aspects of the NASICON materials. I am going to restrict my efforts into the well-known and electrochemically active phases. **Figure 1-6** shows the local environments around Li^+ in the monoclinic and the orthorhombic $Li_3V_2(PO_4)_3$.

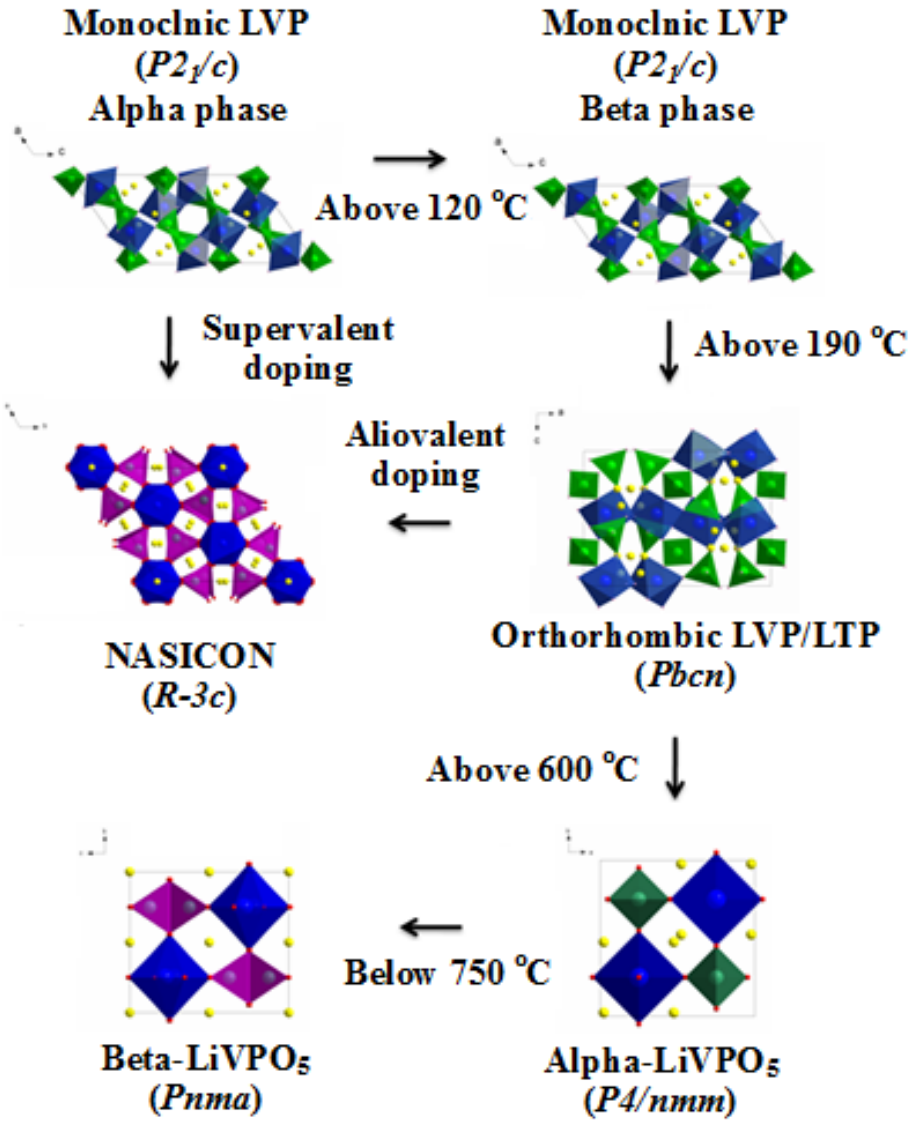

Fig. 1-5 Schematic view of the phase transition pathways to various systems from original NASICON framework. Referenced methodologies were written in parenthesis.

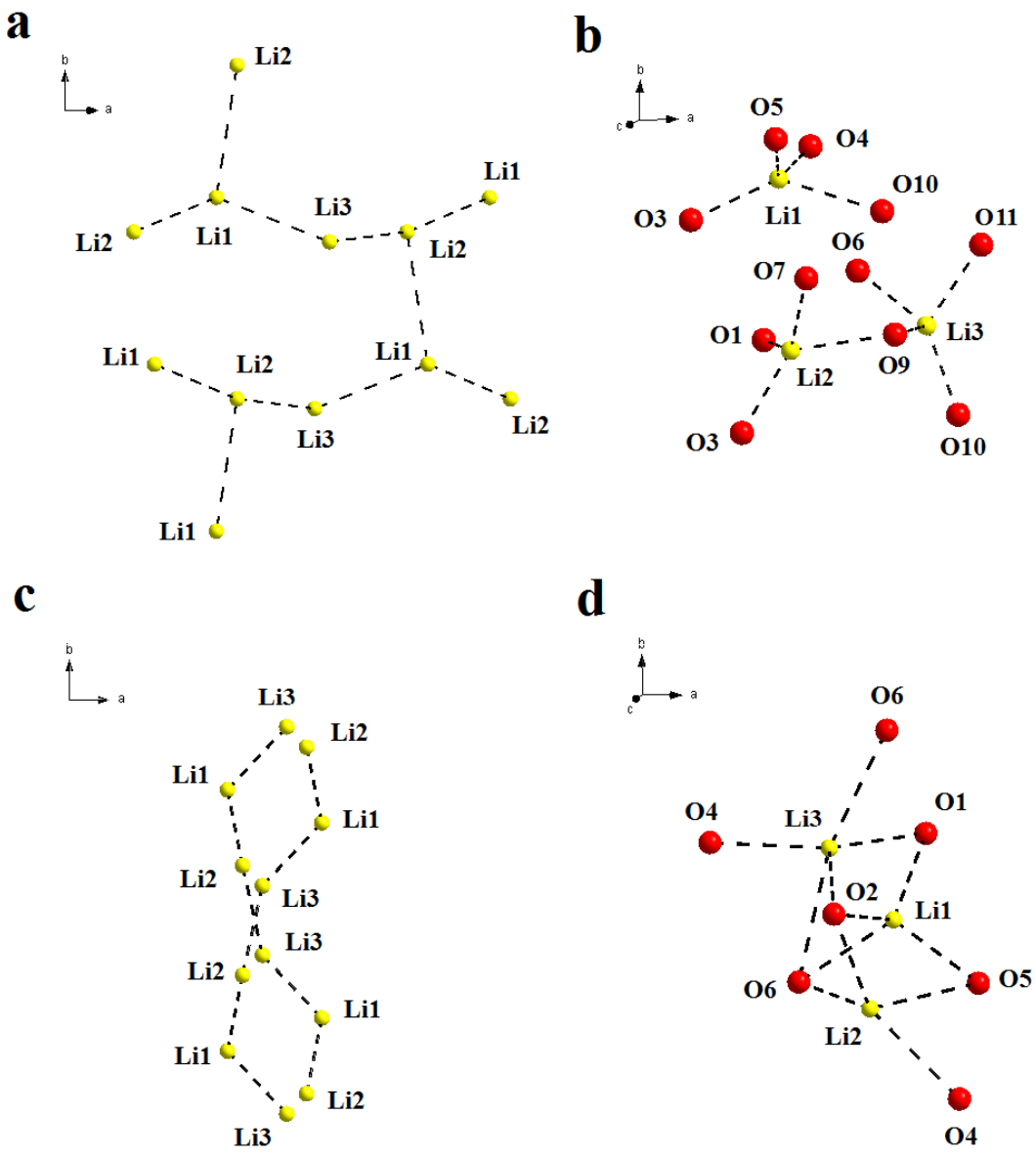

Fig. 1-6 Atomic environments around Li atoms for monoclinic $Li_3V_2(PO_4)_3$ (a, b; ICSD #290299) and orthorhombic $Li_3V_2(PO_4)_3$ (c, d; ICSD #92242).

Table 1-2. Fractional atomic coordinates of monoclinic phase (a, $P2_1/c$; ICSD #290299) and orthorhombic phase (b, *Pbcn*; ICSD #92242). Symmetry operators : (1) x,y,z, (2) x+1/2,-y+1/2,-z, (3) -x,y,-z+1/2, (4) -x+1/2,-y+1/2,z+1/2, (5) -x,-y,-z, (6) -x+1/2,y+1/2,z, (7) x,-y,z+1/2, (8) x+1/2,y+1/2,-z+1/2 for orthorhombic *Pbcn* and (1) x,y,z, (2) -x,y+1/2,-z+1/2, (3) -x,-y,-z, (4) x,-y+1/2,z+1/2 for monoclinic $P2_1/c$.

(a)	*x*	*y*	*z*	**(b)**	*x*	*y*	*z*
Li1	0.1133	0.5883	0.1934	Li1	0.324	0.286	0.285
Li2	0.1891	0.1919	0.2599	Li2	0.3	0.12	0.357
Li3	0.473	0.2213	0.1767	Li3	0.231	0.424	0.27
V1	0.1381	0.5284	0.3897	V1	0.1134	0.247	0.4641
V2	0.3621	0.5389	0.1103	P1	0.1476	0.1067	0.1054
P1	0.0441	0.251	0.0078	P2	0.5	0.0419	0.25
P2	0.4578	0.3975	0.3518	O1	0.3404	0.431	0.1011
P3	0.7519	0.3846	0.1473	O2	0.2732	0.3245	0.4835
O1	0.0267	0.1788	0.0964	O3	0.0312	0.1545	0.0661
O2	0.0361	0.3649	0.4274	O4	0.0741	0.4436	0.3538
O3	0.085	0.0021	0.2803	O5	0.4221	0.1446	0.1582
O4	0.1152	0.633	0.0657	O6	0.1829	0.1583	0.2694
O5	0.1785	0.7151	0.3196				
O6	0.2392	0.3319	0.0704				
O7	0.2789	0.3861	0.3518				
O8	0.3675	0.5514	0.5404				
O9	0.4764	0.2357	0.3141				
O10	0.5906	0.02	0.238				
O11	0.5994	0.4098	0.1688				
O12	0.6748	0.4125	0.0272				

Despite their apparent similarity, the local Li environments appear to be different. Such differences are very important for the electrochemical performance of the corresponding solid state phases. Local environment dictates the forces over the Li^+ when it moves into the crystal lattice. Therefore, intercalation behavior of Li^+ depends on the local environment and should be revealed as precisely as possible.

To the best of our knowledge, systematic investigations on these phases have not yet been performed. So far, monoclinic phase has been predominantly investigated as electrode host because most of the first row transition metals such as Cr, Fe, V, etc. adopt monoclinic crystal structures ($P2_1/c$). This lack of fundamental understanding provides huge motivation to clarify the electrochemical properties of the orthorhombic phase with its unique structure, which is not well understood yet.

Local environments around Li^+ in the monoclinic and orthorhombic $Li_3V_2(PO_4)_3$ shown in **Fig. 1-6** are further revealed in **Table 1-2**, showing the numerical values of the fractional coordinates for all crystallographically different ions in the crystal lattice. In the orthorhombic phase, the occupancies of the Li-ions is competitively changed depending on doping contents or charging states, which make it have high diffusivity and show solid-state reaction.

This stems from large amount of Li-sites in quarter occupancy in the lattice structure with relatively short Li-Li interatomic distances. Thus, the average Li-Li distance in the monoclinic phase is 3.285 Å, while relatively short distance of 1.998 Å is reported for

the orthorhombic phase (ICSD #92242). Second major advantage that makes NASICON-type materials a promising candidate is its various synthesis routes including microwave-assisted carbothermal and co-precipitation. This indicates NASICON-type materials could be easily mass-produced once a condition is optimized as shown in **Table 1-3**.

In addition, NASICON host could be used as not only anode or cathode but also electrolyte by simply substituting the transition metal with electrochemically inactive (non-transition) ones. For example, the substitution of Fe with Ti in $Li_xFe_2(PO_4)_3$ could considerably reduce working potential window of the host and makes it useable as an anode material with large vacant spaces for the Li ions [16]. On the other hand, substituting Ti in $LiTi_2(PO_4)_3$ with Al or Ge makes it work as a solid-state electrolyte. Such feasibilities are beneficial for electrode materials and could considerably reduce production cost and time. In the next chapters, the selected compounds in NASICON-family will be discussed with fundamental idea around their related electrochemical fields.

Table 1-3. Various synthetic routes to prepare NASICON-type materials.

Formula	Precursors	Space group	Method
$Li_3V_2(PO_4)_3$	LiCl, V, P	*P2₁/c*	Flux growth [7]
$Li_3V_2(PO_4)_3$	$LiOH{\cdot}H_2O$, NH_4VO_3, $NH_4H_2PO_4$, citric acid	*P2₁/c*	Spray-drying [8]
$Li_3V_2(PO_4)_3$	LiH_2PO_4, V_2O_5, sucrose, ethanol	*P2₁/n*	Microwave [9]
$Li_{1.5}Ti_2(PO_4)_3$	$LiOH{\cdot}H_2O$, $Ti[OCH(CH_3)_2]_4$, $NH_4H_2PO_4$, citric acid	*Pbcn*	Sol-gel [10]
$Li_2Ti_2(PO_4)_3$	LiCl, Ti, P	*Pbcn*	Flux growth [11]
$LiTi_2(PO_4)_3$	Li_2CO_3, TiO_2, $NH_4H_2PO_4$	*R-3c*	Solid-state [12]
$Na_3Zr_{2/3}Fe_{4/3}(PO_4)_3$	NaOH, $ZrO(NO_3)_2$, $(NH_4)_2HPO_4$, $Fe(NO_3)_3$	*R-3c*	Co-precipitation [13]
$Na_3V_2(PO_4)_3$	Na_2CO_3, NH_4VO_3, $NH_4H_2PO_4$, citric acid	*R-3c*	Spray-pyrolysis [14]
$Na_3V_2(PO_4)_3$	Na_2CO_3, V_2O_5, $NH_4H_2PO_4$, ascorbic acid, PEG	*R-3c*	Hydrothermal [15]

1.3. Basics

1.3.1 Structural determinations

To understand and define the electrode system, it is essential to classify the compound and refine its electronic structure. Space groups are categorized as 7 lattice systems: Triclinic, monoclinic, orthorhombic, tetragonal, rhombohedral, hexagonal, and cubic, which are combinations of 32 crystallographic point groups with 14 Bravais lattices. Here, Bravais lattice is an infinite array of discrete points generated by a set of discrete translation operations:

$$R = n_1 a_1 + n_2 a_2 + n_3 a_3 \qquad (1.1)$$

where n_i are any integers and a_i are the primitive vectors which lie in different directions and span the lattice [17-19]. Each space group has unique arrangements and conditions to fulfill to be determined could be observed using X-ray diffraction information. For example, diffracted X-ray beam follows well-known Bragg's Law ($n\lambda = 2d_{hkl} \sin \theta$), providing special d-spacing values, which are vector drawn from origin of the unit cell to plane (*hkl*) at 90 ^{o}. An array of such diffraction peaks has certain order and could roughly be matched by following relations:

Cubic $\frac{1}{d^2} = \frac{h^2 + k^2 + l^2}{a^2}$ (1.2)

Tetragonal $\frac{1}{d^2} = \frac{h^2 + k^2}{a^2} + \frac{l^2}{c^2}$ (1.3)

Orthorhombic $\frac{1}{d^2} = \frac{h^2}{a^2} + \frac{k^2}{b^2} + \frac{l^2}{c^2}$ (1.4)

Hexagonal $\frac{1}{d^2} = \frac{4}{3}\left(\frac{h^2 + hk + k^2}{a^2}\right) + \frac{l^2}{c^2}$ (1.5)

Monoclinic $\frac{1}{d^2} = \frac{1}{\sin^2\beta}\left(\frac{h^2}{a^2} + \frac{k^2\sin^2\beta}{b^2} + \frac{l^2}{c^2} - \frac{2hl\cos\beta}{ac}\right)$ (1.6)

Triclinic

$$\frac{1}{d^2} = \frac{1}{V^2}(h^2b^2c^2\sin^2\alpha + k^2a^2c^2\sin^2\beta + l^2a^2b^2\sin^2\gamma + 2hkabc^2(\cos\alpha\cos\beta - \cos\gamma) + 2kla^2bc\left(\cos\beta\cos\gamma - \cos\alpha\right) + 2hlab^2c\,(\cos\alpha\cos\gamma - \cos\beta))$$

$$V = abc\,(1 - \cos^2\alpha - \cos^2\beta - \cos^2\gamma + 2\cos\alpha\cos\beta\cos\gamma)^{0.5} \quad (1.7)$$

Once this initial fitting is done, we need to classify reflection conditions and systematic absences to determine its space group from the highest possible supergroup to lowest subgroups. Thanks to the development of computer science, now non-

crystallographers could easily estimate possible space group without manual fitting and matching using software such as SHELXS97 based on direct methods. The problem becomes complicated when only powder X-ray diffraction pattern is available, because the diffraction peaks from different planes and atoms could be overlapped and represented as one peak in designated 2θ. However, the powder X-ray diffraction pattern itself may be challenging when it comes to structural determination because of difficulty in observation of subtle peaks that are indicative of either reflection conditions or systematic absences of the crystal system. The powder diffraction pattern is usually represented by ring-shaped pattern in XRD due to the contribution from randomly oriented single crystals.

In this case, we need to assign proper (*hkl*) on each diffraction ring. According to the Laue condition, diffraction occurs when vector of diffraction wave, *K*, is equal to the vector of reciprocal lattice, g_{hkl} ($K = g_{hkl}$). Therefore, we need to find a reciprocal lattice of a zone axis [*uvw*], which meets Laue condition to index diffraction patterns. If zone [*uvw*] contains two random planes ($h_1k_1l_1$) and ($h_2k_2l_2$), the direction of intersection of these two planes become the zone axis [*uvw*] and can be obtained using zone law as follows:

$$h_1u + k_1v + l_1w = 0,\ h_2u + k_2v + l_2w = 0 \qquad (1.8)$$

$$\begin{bmatrix} u & v & w \\ h_1 & k_1 & l_1 \\ h_2 & k_2 & l_2 \end{bmatrix} = 0 \qquad (1.9)$$

$$u : v : w = \begin{bmatrix} k_1 & l_1 \\ k_2 & l_2 \end{bmatrix} : (-1) \times \begin{bmatrix} h_1 & l_1 \\ h_2 & l_2 \end{bmatrix} : \begin{bmatrix} h_1 & k_1 \\ h_2 & k_2 \end{bmatrix} \qquad (1.10)$$

$$u = k_1l_2 - k_2l_1 \; ; \; v = h_2l_1 - h_1l_2 \; ; \; w = h_1k_2 - h_2k_1 \qquad (1.11)$$

where $hu + kv + lw = 0$, and $\overrightarrow{g_{hkl}} = h\vec{a} + k\vec{b} + l\vec{c}$. The addition rule for these vector values allow following relations with two points in reciprocal space:

$$\vec{g}_{h1k1l1} + \vec{g}_{h2k2l2} = \vec{g}_{(h1+h2)(k1+k2)(l1+l2)} \qquad (1.12)$$

$$\cos p = \frac{\vec{g}_{h1k1l1} \times \vec{g}_{h2k2l2}}{|\vec{g}_{h1k1l1}| \times |\vec{g}_{h2k2l2}|} \qquad (1.13)$$

where p is angle between plane ($h_1k_1l_1$) and ($h_2k_2l_2$), $\vec{g}_{h1k1l1} = h_1\overrightarrow{a} + k_1\vec{b} + l_1\vec{c}$, and $\vec{g}_{h2k2l2} = h_2\overrightarrow{a} + k_2\vec{b} + l_2\vec{c}$. This becomes a bit challenging especially if the pattern is incorporated with peak broadening or microstrain effects. In general, peak broadening due to small crystalline size is usually estimated by means of the famous Scherrer equation [19]:

$$\tau = K\lambda / \beta \cos\theta \qquad (1.14)$$

where τ is mean size of crystalline size, K is shape factor, which is normally about 0.9, λ is wavelength of X-ray, and β is line broadening at FWHM. However, when both size broadening (β_L) and strain broadening (β_e) occur as follows:

$$\beta_L = K\lambda / (L\cos\theta), \quad \beta_e = C\varepsilon \tan\theta \qquad (1.15)$$

where C (~4) is constant for inhomogeneous strain. These effects must be determined by convolution, which was assumed to be simple sum of these two effects by Williamson and Hall:

$$\beta_{tot} = \beta_e + \beta_L = C\varepsilon \tan\theta + K\lambda / (L\cos\theta) \qquad (1.16)$$

multiplying by $\cos\theta$ transforms this equation to a standard form of the linear equation ($y = mx + c$):

$$\beta_{tot}\cos\theta = C\varepsilon \sin\theta + K\lambda/L \qquad (1.17)$$

where slope m ($C\varepsilon$) which relates to strain component and the intercept ($K\lambda/L$) which relates to size component could be obtained by plotting $\beta_{tot}\cos\theta$ vs. $\sin\theta$. In this relation, we could plug in each θ value with intensity and predict the thickness of the crystallites along special (*hkl*) direction. For example, (100) point existing above the mean straight line suggests that powder crystalline is thinnest along (100) direction [20]. On the other hand, each diffraction peak has its unique intensity depending on the crystal system, because each peak is the summation of all atoms scattering in certain (*hkl*) plane. This value is, therefore, determined by location and types of atoms on the planes as follows:

$$I_{hkl} \propto |F_{hkl}|^2 \tag{1.18}$$

$$F_{hkl} = \sum_{j=1}^{m} N_j f_j \exp[2\pi i(hx_j + ky_j + lz_j)] \tag{1.19}$$

where F_{hkl} is structure factor, x_j, y_j, and z_j are fractional coordinates, f_j is temperature-dependent atomic scattering factor for each atom, and N_j is fraction of every position that is occupied by atoms. In practice, the calculated structure factor in terms of the model based on point scatters whose atomic positions are smeared out by thermal motions could be described as follows [21]:

$$F_{hkl} = \sum_{j=1}^{n} b_j N_j \exp\left[2\pi i\left(hx_j + ky_j + lz_j\right)\right] \exp(-\mathrm{B_j}\sin^2\theta\lambda^2) \qquad (1.20)$$

where F is vector with both amplitude of F and phase φ, b_j is stationary scattering factor for each atom, and B is $8\pi^2\langle u^2\rangle$, where $\langle u^2\rangle$ is the root mean square displacement of the atom from its average position. In general, tightly bound atoms have low thermal displacement parameters, which indicate that the designated atoms have small vibrational motions. This also means that we can expect high ionic performances of Li or Na ions when they have higher displacement parameters and could expect structural stability when other elements have low displacement parameters. The structure factor is the Fourier transform of the electron density, $\rho(x,y,z)$, taken over the entire unit cell and thus:

$$F_{hkl} = \int_0^c \int_0^b \int_0^a \rho(x,y,z) \exp[2\pi i(hx + ky + lz)]\, dx\, dy\, dz \qquad (1.21)$$

The initial model is usually fitted with atomic coordinates with corresponding isotropic displacement parameters for scattering density, $\rho(x,y,z)$, and this value could be calculated using reverse Fourier transform in following relation:

$$\rho(x,y,z) = \sum_{hkl} F_{hkl} \exp[-2\pi i\ (hx + ky + lz)]/\ V \qquad (1.22)$$

and difference Fourier map allows us to find missing atoms in the model structure and can be obtained using following relation:

$$\rho(x,y,z) = \sum_{hkl}[F_{hkl}(\text{obs}) - F_{hkl}(\text{cal})]\ \exp[-2\pi i\ (hx + ky + lz)]/\ V \quad (1.23)$$

Since it is not possible to measure *F*(obs), it is only possible to assign correct model structure to make *F*(obs) and *F*(cal) the same where strong reflections are observed. There are several indicators that verify the reliability of refined model structure. The universally accepted values are as follows:

$$R_p = \frac{\sum |\ Y_{\text{obs}} - Y_{\text{cal}}\ |}{\sum |\ Y_{\text{obs}}|} \text{ x } 100\% \quad (1.24)$$

$$wR = \left(\frac{\sum |\ w|\ Y_{\text{obs}} - \ Y_{\text{cal}}|^2|}{\sum |\ wY_{\text{obs}}^2|}\right)^{0.5} \text{ x } 100\% \quad (1.25)$$

$$R_B = \frac{\sum |\ I_{\text{obs}} - \ I_{\text{cal}}\ |}{\sum |\ I_{\text{obs}}|} \text{ x } 100\% \quad (1.26)$$

$$R_{exp} = \left(\frac{N - P + C}{\sum_i w_i y_i(\text{obs})^2}\right)^{0.5} \text{ x } 100\% \quad (1.27)$$

$$\chi^2 = (R_{wp} / R_{exp})^2 \qquad (1.28)$$

where N is total number of observations, P is the number of refined parameters, C is the number of constraints used in the refinement, and Y is F^2, F, or I. Interestingly, allocations of all elements give us important information about interatomic distances which are related to bond lengths and valence states. It is widely known that the decrease of bond valence, $S_{A\text{-}X}$ with bond length $D_{A\text{-}X}$ between a cation A and an anion X could be represented as following equation:

$$S_{A\text{-}X} = \exp[(D_0 - D_{A\text{-}X})/b] \text{ or } S_{A\text{-}X} = (D_0/ D_{A\text{-}X})^N \qquad (1.29)$$

where, D_0, b, and N are empirical parameters selected to assure expectancy value for bond-valence sum, $V(A)$, of the cation A for all bonds to its coordinated anions, X, as follows:

$$V(A) = \sum_X S_{A-X} \qquad (1.30)$$

And bond-valence deviation could be represented as follow:

$$\Delta S_{A\text{-}X} = |\exp[(D_{A\text{-}X} - D_0)/b] - S_{\text{ideal}}| \qquad (1.31)$$

where S_{ideal} is contribution from a single bond to total valence sum $V(A) = V_{\text{ideal}}(A)$. However, parameters b and D_0 are usually difficult to obtain. The parameter b could be calculated from a softness of a bond. The individual particles could be described using their chemical potential, μ, and absolute hardness, η, which are defined as follows [22]:

$$\mu = (\partial E / \partial N)_v \text{ and } \eta = 0.5(\partial \mu / \partial N)_v = 0.5(\partial^2 E / \partial N^2)_v \qquad (1.32)$$

where v is potential of nucleus and N is number of electrons and when the particle is neutral, these values could be obtained using relationship between ionization energy, I_E, and electron affinity, E_A, as follows [23]:

$$-\mu \approx (I_E + E_A)/2 = x_{ab},\ \eta \approx (I_E - E_A)/2 = 1/\sigma \qquad (1.33)$$

where x_{ab} is absolute electronegativity and σ is absolute softness. The value b could roughly be related to difference between softness of anion and cation and negligible correlation with sum of softness of anion and cation [24]. The universal value of 0.37 Å is generally assigned for b, while $D_0(ij)$ could be interpreted as the sum of atomic radii

of atoms *i* and *j* [25, 26]:

$$D_0(ij) = D_i + D_j - [D_i D_j (x_i^{0.5} - x_j^{0.5})/(x_i D_i + x_j D_j)] \quad (1.34)$$

1.3.2 Diffusion coefficient

To evaluate electrochemical property of one electrode system, diffusivity (*D*) is one of the most important terms along with one's electrical conductivity. Following relation could be stated by combining Faraday's law and Fick's first law:

$$i_p = nFAD\,(dC/dx)_0 \qquad (1.35)$$

where *n* is number of electron, *F* is Faraday's constant, *A* is the electrode area, and *dC*/*dx* is concentration gradient. When the potential sweeps by formal potential, it is either oxidized or reduced by electrode and generates concentration gradient, which is proportional to current. The peak current (i_p) could be observed when potential sweeps and could be expressed as following Randles-Sevcik equation:

$$i_p = 0.4463\,nFAC\,(nFvD/RT)^{0.5} \qquad (1.36)$$

where *n* is the number of electron, *v* is the potential sweep rate (V/s), *F* is Faraday's constant, *A* is the electrode area, 0.4463 is Randles-Sevcik constant, *R* is the gas constant, and *T* is the absolute temperature. This equation is valid only when the redox system remains in equilibrium state. Therefore, various scan rates should be applied to estimate current versus potential plot and the resulting values should be plugged into the

equation. Another viable way of obtaining diffusion coefficient is by GITT (Galvanostatic Intermittent Titration Technique), which uses galvanostatic pulses instead of various current rates and can be represented by following relation:

$$D_{\mathrm{GITT}} = \frac{4}{\pi}\left(\frac{iV_m}{Z_A FS}\right)^2 \left\{\frac{\left(\frac{dE}{d\delta}\right)}{\left(\frac{dE}{d\sqrt{t}}\right)}\right\}^2 \qquad (1.37)$$

where V_m is the molar volume of electrode (cm^3/mol), Z_A is charge number, S is surface area (cm^2), $\left(\frac{dE}{d\delta}\right)$ is the slope of the coulometric titration curve, which is found by plotting the steady-state voltages E(V) measured after each titration step δ, and $\left(\frac{dE}{d\sqrt{t}}\right)$ is the slope of the linearized plot of the potential E(V) during the current pulse of duration t seconds.

In a typical GITT experiment sufficiently small current steps are applied for short intervals in a way allowing us to consider $\frac{dE}{d\sqrt{t}}$ linear. Therefore, the coulometric curve can also be considered linear over the composition range involved in that step. Under these assumptions [27-29] eq. 1.37 simplifies to:

$$D_{\mathrm{GITT}} = \frac{4}{\pi\tau}\left(\frac{n_m V_m}{S}\right)^2 \left(\frac{\Delta E_s}{\Delta E_t}\right)^2 \qquad (1.38)$$

where τ stands for the duration of the current pulse (s), n_m is the number of moles (mol), ΔE_s is steady-state voltage change due to the current pulse, and ΔE_t is voltage change during the constant current pulse. These values are shown in **Fig. 1-7**. Comparing equations 1.37 and 1.38 yields the relationship:

$$\frac{n_m}{\tau} = \frac{i}{Z_A F} \text{ dimension } \frac{\frac{\text{Coulomb}}{\text{s}}}{\frac{\text{Coulomb}}{\text{mol}}} = \frac{\text{mol}}{\text{Coulomb}} \qquad (1.39)$$

Reports regarding the diffusivity of NASICON-framework materials are scare regardless it is one of the most important factors that determine the electrochemical performance of the electrode materials. In this context, investigation of diffusivity for the seemingly the same materials: orthorhombic $Li_{1.5}Ti_2(PO_4)_3$ as compare to well-known rhombohedral $LiTi_2(PO_4)_3$ would be treated to explain differences in the electrochemistry, which is important for understanding missing connection between crystallography and electrochemistry for NASICON family.

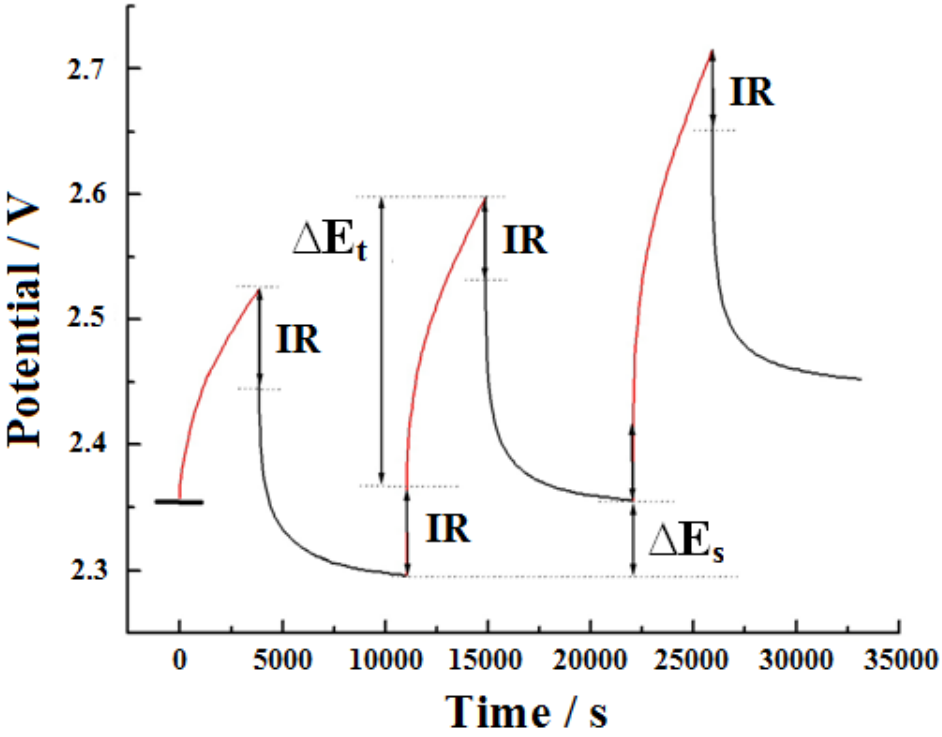

Fig. 1-7 Practically measured parameters during GITT experiment. ΔE_s and ΔE_t are fed into eq. 1.38.

References

[1] Y. Kee and H. Yun, *Acta Cryst.*, *E***69** (2013) i11.

[2] A. B. Bykov, A. P. Chirkin, L. N. Demyanets, S. N. Doronin, E. A. Genkina, A. K. Ivanovshits, I. P. Kondratyuk, B. A. Maksimov, O. K. Mel'nikov, L. N. Muradyan, V. I. Simonov, and V. A. Timofeeva, *Solid State Ionics*, **38** (1990) 31.

[3] J. E. Iglesias and C. Pecharrom´an, *Solid State Ionics*, **112** (1998) 309.

[4] M. Sato, H. Ohkawa, K. Yoshida, M. Saito, K. Uematsu, and K. Toda, *Solid State Ionics*, **135** (2000) 137.

[5] Y. Kee, N. Dimov, E. Kobayashi, A. Kitajou, and S. Okada, *Solid State Ionics*, **272** (2015) 138.

[6] X. Yupeng, Z. Yanhui, and S. Zhi, *J. Alloys. Compd*., **628** (2015) 396.

[7] Y. Kee, N. Dimov, K. Minami, and S. Okada, *Electrochim. Acta*, **174** (2015) 516.

[8] Y. Kee, S. Lee, and H. Yun. *Acta Cryst.*, *E***67** (2011) i49.

[9] G. X. Wang, D. H. Bradhurst, S. X. Dou, and H. K. Liu, *J. Power Sources*, **124** (2003) 231.

[10] A. Ignaszak, P. Pasierb, R. Gajerski, and S. Komornicki, *Thermochim. Acta*, **426** (2005) 7.

[11] J. Mao, C. Luo, T. Gao, X. Fan, and C. Wang, *J. Mater. Chem.*, *A* **3** (2015) 10378.

[12] W. Duan, Z. Zhu, H. Li, Z. Hu, K. Zhang, F. Cheng, and J. Chen, *J. Mater. Chem.*, *A* **2** (2014) 8668.

[13] M. Park, X. Zhang, M. Chung, G. B. Less, and A. Sastry, *J. Power Sources*, **195** (2010) 7904.

[14] P. Han, Y. Zhu, and J. Liu, *J. Power Sources*, **284** (2015) 459.

[15] Y. Inda, T. Katoh, and M. Baba, *J. Power Sources*, **174** (2007) 741.

[16] S. Patoux, G. Rousse, J. Leriche, and C. Masquelier, *Solid State Science*, **6** (2004) 1113.

[17] A. Mois I, U. Müller, H. Wondratschek. International Tables for Crystallography. Vol. A1. Springer, 2006.

[18] K. Charles, Introduction to Solid State Physics, Seventh ed. ISBN 0-471-11181-3. New York: John Wiley & Sons, 1996.

[19] B. Harold, B. Rolf, N. Joachim, W. Hans, Z. Hans, Crystallographic groups of four-dimensional space, ISBN 978-0-471-03095-9. New York:Wiley-Interscience [John Wiley & Sons], 1978.

[20] P. Scherrer, *Göttinger Nachrichten Gesell*, **2** (1918) 98.

[21] M. Attfield, P. Barnes, J. Cockcroft, and H. Driessen, Advanced certificate in powder diffraction on the web. School of Crystallography, Birkbeck college, University of London, 2006.

[22] I. Brown and D. Altermatt, *Acta Cryst., B***41** (1985) 244.

[23] R. G. Parr and R. G. Pearson, *J. Am. Chem. Soc.*, **105** (1983) 7512.

[24] S. Adams, *Acta Cryst., B***57** (2001) 278.

[25] N. K. Ray, L. Samuels, and R. G. Parr, *J. Chem. Phys*., **70** (1979) 3680.

[26] M. O'Keeffe and N. E. Brese, *J. Am. Chem. Soc*., **113** (1991) 3226.

[27] C. J. Wen, B. A. Boukamp, R. A. Huggins, and W. Weppner, *J. Electrochem. Soc*., **126** (1979) 2258.

[28] W. Weppner and R. A. Huggins, *J. Electrochem. Soc*., **124** (1977) 1569.

[29] Y. Zhu and C. Wang, *J. Phys. Chem., C* **114** (2010) 2830.

CHAPTER 2

Structural and Electrochemical Properties of Al- and Fe-doped $Li_3V_2(PO_4)_3$ for All-solid-state Symmetric Lithium Ion Batteries Prepared by Spray-drying-assisted Carbothermal Method

2.1. Introduction

Aprotic liquid electrolytes, which are comprised of electrolyte salt such as $LiPF_6$ dissolved in the organic solvents such as ethylene carbonate (EC) and dimethyl carbonate (DMC), have been known as one of the best electrolytes in Li-ion battery industries due to their high ionic conductivity. However, electrolyte salts and organic solvents decompose at elevated temperature (>200 °C) and generate strong Lewis acid PF_5 and other gases such as CH_4 and CO_2. In addition, the high costs and the environmental hazards of current organic electrolytes have all seriously hindered the commercialization of large-scale Li ion batteries.

As a possible alternative, all-solid-state batteries with inorganic solid-state electrolyte, which also acts as separator, have been suggested as one of the safest possible future lithium-ion energy storage systems. Although ionic conductivities of general solid-state electrolytes are approximately 3-6 orders of magnitude lower than those of organic electrolytes as listed in **Table 2-1** [1], they have been widely investigated for future uses. The main groups of the reported solid-state electrolytes are listed in **Table 2-2** [1] and previously reported all-solid-state batteries using solid-state electrolytes are listed in **Table 2-3**. These comparably low ionic conductivities of solid-state electrolytes are because the electrolyte is solid, allowing ions to diffuse or conduct through designed channels in the lattice.

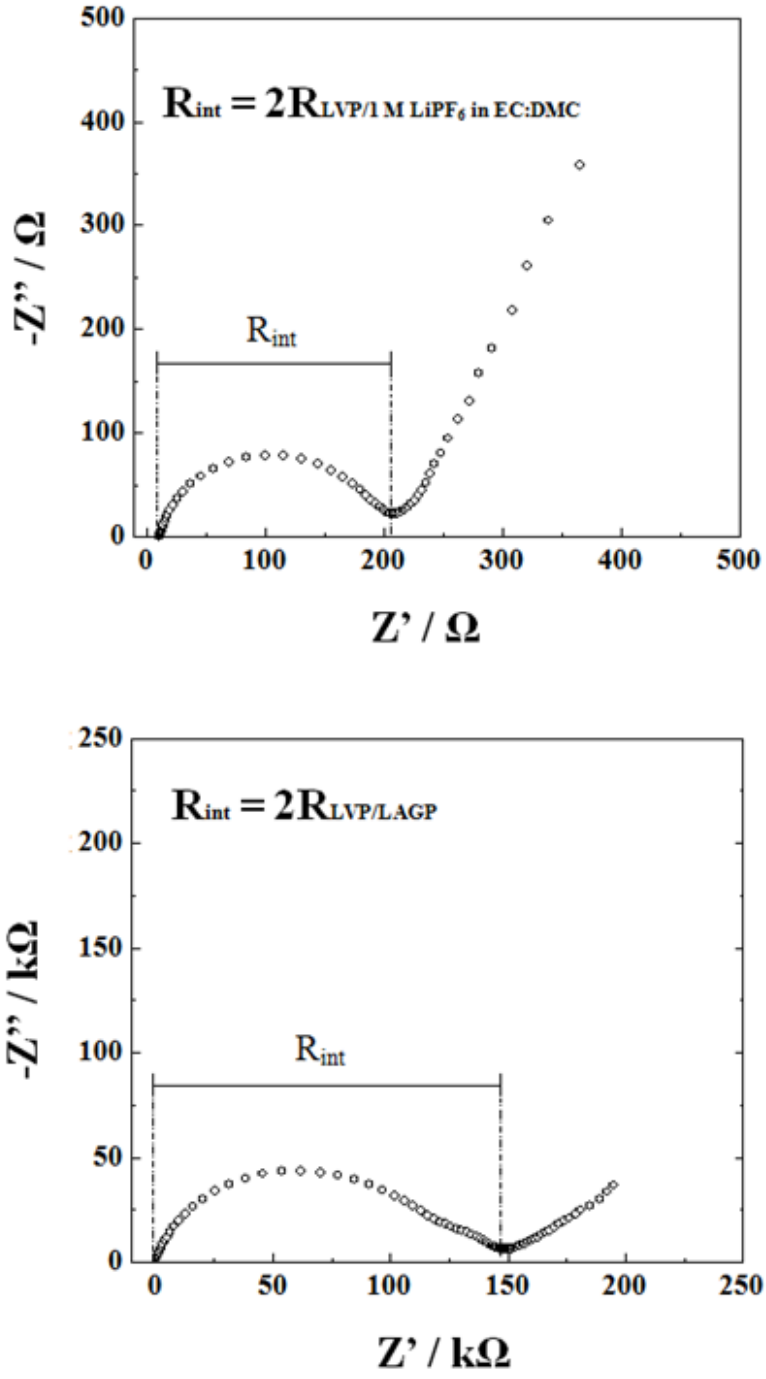

Fig. 2-1 Nyquist plots of $Li_3V_2(PO_4)_3$ symmetric cell using 1 M $LiPF_6$ in EC:DMC (1:1 in volume) as electrolyte or $Li_{1.5}Al_{0.5}Ge_{1.5}(PO_4)_3$ solid-state electrolyte in the frequency range between 10 mHz and 1 MHz with an AC signal of 10 mV at room temperature.

Table 2-1. The ionic conductivity comparison between organic and solid-state electrolytes at room temperature.

Liquid electrolyte	**Ionic conductivity**	**Solid-state Electrolyte**	**Ionic conductivity**
1 M $LiClO_4$ (PC)	5.6 S cm^{-1}	$Li_5La_3Ta_2O_{12}$	5×10^{-5} S cm^{-1}
1 M $LiAsF_6$ (EC/DMC)	11.1 S cm^{-1}	$30P_2S_5$–$70Li_2S$	1.0×10^{-3} S cm^{-1}
1 M $LiPF_6$ (EC/DMC)	10.7 S cm^{-1}	$Li_{1.3}Al_{0.3}Ge_{1.7}(PO_4)_3$	3.99×10^{-4} S cm^{-1}
1 M $LiBF_4$ (PC)	1.7 S cm^{-1}	$10LaAlO_3$-$90La_{0.5}Li_{0.5}TiO_3$	1×10^{-3} S cm^{-1}

Table 2-2. Previously reported solid-state electrolytes.

Class	Type	Formula	Ionic conductivity
Polymeric	Wet-polymer	$LiPF_6$ 20wt% in PVdF	2.7×10^{-4} S cm^{-1}
	Plastic crystal	$4LiBF_4$-96Succinonitrile	1.0×10^{-4} S cm^{-1}
Crystalline	Perovskite	$xLaAlO_3$-(1-x)$La_{0.5}Li_{0.5}TiO_3$ (x = 0, 0.1)	1.0×10^{-3} S cm^{-1}
	Garnet	$Li_6BaLa_2Ta_2O_{12}$	5.0×10^{-3} S cm^{-1}
	Glassy-NASICON	$Li_{1.3}Al_{0.3}Ge_{1.7}(PO_4)_3$	3.99×10^{-4} S cm^{-1}
Glassy	Sulfide-based	$0.375SiS_2$-$0.375Li_2S$-0.25LiCl	1.2×10^{-4} S cm^{-1}
	Glass-ceramics	$30P_2S_5$-$70Li_2S$	1.0×10^{-3} S cm^{-1}

Table 2-3. Reported all-solid-state batteries.

Cathode	Solid-state electrolyte	Anode	Initial capacity
$LiFePO_4$	PEG/KH560-LiTFSI	Li	156.7 mAh g^{-1} at 120°C (1 C) [2]
$LiCoO_2$	$Li_{1+x+y}Al_xTi_{2-x}Si_yP_{3-y}O_{12}$	$Li_4Ti_5O_{12}$	150 mAh g^{-1} at 60°C (1/12 C) [3]
$LiFePO_4$	$80Li_2S$-$20P_2S_5$	In	110 mAh g^{-1} at 50°C (13 μA cm^{-2}) [4]
$Li_3V_2(PO_4)_3$	$Li_{1.5}Al_{0.5}Ge_{1.5}(PO_4)_3$	$Li_3V_2(PO_4)_3$	92 mAh g^{-1} at 25°C (8.8 μA cm^{-2}) [5]
$LiMn_2O_4$	$80Li_2S$-$20P_2S_5$	In	55 mAh g^{-1} at 25°C (0.064 mA cm^{-2}) [6]

This disadvantage gives rise to intrinsically high interfacial resistance between electrode and solid-state electrolyte. As illustrated in **Fig. 2-1**, interfacial resistance between solid-state electrolyte and electrodes prepared under general method such as hot-pressing is 2-3 orders of magnitude larger than that between organic electrolyte and electrodes. On the other hand, there have not been many efforts for electrode materials in terms of all-solid-state cells as Li-ion diffusion kinetics of electrode materials were regarded as less determining factor for cell designs as compare to conduction kinetics of solid-state electrolytes.

Therefore, there is still a room for improvement via careful screening and preparation for electrode materials. One of the most interesting materials in this case is lithium vanadium phosphate, $Li_3V_2(PO_4)_3$, which is one of the most promising candidates as both cathode and anode, allowing the following reactions:

$$Li_3V_2(PO_4)_3 \rightarrow LiV_2(PO_4)_3 + 2Li^+ + 2e^- \text{ (Up to 4.2 V vs. } Li/Li^+)$$

$$Li_3V_2(PO_4)_3 + 2Li^+ + 2e^- \rightarrow Li_5V_2(PO_4)_3 \text{ (Down to 1.5 V vs. } Li/Li_+)$$

On the other hand, like other polyanion hosts, the strong inductive effect from the PO_4 polyanion groups seriously decreases the electronic conductivity. In order to improve the rate capability and thus to utilize $Li_3V_2(PO_4)_3$ under practically interesting

recharge rates, the electronic conductivity of $Li_3V_2(PO_4)_3$ should be increased. Here, the electrical conductivity is an ability to conduct an electric current and could be obtained from following relation:

$$\rho = 1/\sigma = R\,(A/l) \qquad (2.1)$$

where ρ is the electrical resistivity, R is the electrical resistance of a certain material (ohm), l is the length of material (m or cm), and A is the cross-sectional area of the conductor where the current flows (m^2 or cm^2). This electrical conductivity has been reportedly high for a metal with high number of valence electrons and could be determined by a few factors as follows [7]:

$$\rho_{tot} = 1/\sigma_{tot} = \rho_T + \rho_I + \rho_D \qquad (2.2)$$

where ρ_T is temperature dependent resistivity (= $\rho_0 + aT$), ρ_I is impurity dependent resistivity (= $Ac_i(1\text{-}c_i)$), and ρ_D is resistivity from deformation-induced point defects. The electrical conduction is rather simple in the metal because electrons can be promoted above Fermi level, which could be controlled by manipulating above factors. However, in semiconductor, electrons need to jump above the band gap to conduct, and thus it is much more difficult to control and determine electrical conductivity, which

could be described as follows:

$$\sigma = n|e|\mu_e + p|e|\mu_h \qquad (2.3)$$

where n is number of conduction electrons per unit volume, p is number of holes in valence band per unit volume, and μ is mobility of either holes in valence band or electrons in conduction band. Two simple ways to increase electrical conductivity of semiconductor are either to produce a large amount of additional conduction electrons near conduction band ($\sigma \sim n|e|\mu_e$) or produce a large amount of holes on just above valence band ($\sigma \sim p|e|\mu_h$). In the low level of doping (E_c-$E_v \sim$ constant), electron and hole carrier concentrations could be expressed by using Maxwell-Boltzmann statistics as follows [8]:

$$n_e = N_c(T)\exp[(E_f - E_c)/kT] \text{ and } n_h = N_v(T)\exp[(E_v\text{-}E_f)/kT] \qquad (2.4)$$

$$N_c(T) = 2(2\pi m_e kT/h^2)^{3/2} \text{ and } N_v(T) = 2(2\pi m_h kT/h^2)^{3/2} \qquad (2.5)$$

where E_f is Fermi level, E_c is the minimum energy of the conduction band, E_v is the maximum energy of the valence band, k is Boltzmann constant, m_e and m_h are density of states effective masses of electrons and holes, respectively. Although doping mechanism

of semiconductor is rather complicated, because band bending occurs in the forms of Schottky junction or ohmic junction, several efforts to increase its intrinsic electrical conductivity by doping or carbon-coating have been tried.

Table 2-4 lists different electrochemical performances of $Li_3V_2(PO_4)_3$ by various carbon sources, which is very interesting because electrochemical performance is not only dependent on carbon-coating but carbon source [9]. In addition, **Table 2-5** lists various attempts to improve electrochemical properties of $Li_3V_2(PO_4)_3$ by doping transition metals, which considerably stabilize the initial structure and increase electronic conductivities. However, in many cases attempts to dope the parent $Li_3V_2(PO_4)_3$ structure do not succeed. For example, when a small amount of iron is added as a dopant, olivine $LiFePO_4$ is typically incorporated into $Li_3V_2(PO_4)_3$ as impurity phase [14]. During my preliminary screening, doping of molybdenum on monoclinic $Li_3V_2(PO_4)_3$ was initially tried assuming trivalent molybdenum may be partially substituted with vanadium because molybdenum could have various valence ranging from +2 to +6 in the working voltage area, which makes $Li_3V_{2-x}Mo_x(PO_4)_3$ could extract all 3 Li from the lattice structure.

However, the synthetic results indicated that molybdenum could actually also be doped on phosphorus sites, not only vanadium sites, which seriously decreased the specific capacity of the pristine material. Therefore, iron which is the cheapest transition metal and aluminum which is well-known structural stabilizer with valence of +III are

chosen as dopants in this study. As a rule of thumb, the doping amount in this study is set to be 5% because i) higher amount of structural stabilizer atoms reduce the amount of redox couples and ii) lower amount of structural stabilizer has very small effects on both electrochemical charge/discharge properties and structures. To assure the quality of final products, a spray-drying-assisted carbothermal synthesis method, which is suitable for large-scale production of homogeneous materials composed of spherical particles, was applied to isolate a single phase of Fe-doped and Al-doped $Li_3V_2(PO_4)_3$. In addition, all-solid-state symmetric Li-ion batteries with Al- and Fe-doped monoclinic $Li_3V_2(PO_4)_3$ cathode/anode were assembled and compared to the all-solid-state symmetric Li-ion batteries with pristine $Li_3V_2(PO_4)_3$ cathode/anode at room temperature.

Table 2-4. Electrochemical performances of Carbon-coated monoclinic $Li_3V_2(PO_4)_3$.

Carbon source	Carbon content	Voltage	Current rate	Capacity (1^{st})	Reference
Starch	3.45 wt%	3.0-4.3 V	0.1 C	130 mAh g^{-1}	[10]
Sucrose	5 wt%	3.0-4.8 V	0.1 C	145 mAh g^{-1}	[11]
Citric acid	4.1 wt%	2.5-4.5 V	0.1 C	161.3 mAh g^{-1}	[12]
Glucose	4.8 wt%	3.0-4.5 V	0.2 C	127.8 mAh g^{-1}	[13]
Oleic acid	2 wt%	3.0-4.3 V	1 C	131 mAh g^{-1}	[14]
Glycine	8 wt%	3.0-4.3 V	1 C	125.4 mAh g^{-1}	[15]
Ascorbic acid	1.72 wt%	3.0-4.8 V	10 C	106.6 mAh g^{-1}	[16]

Table 2-5. Electrochemical performances of M-doped monoclinic $Li_3V_2(PO_4)_3$.

Material	Voltage	Current rate	Capacity (1st)	Reference
$Li_3V_{1.98}Al_{0.02}(PO_4)_3$	3.0-4.8 V	0.1 C	187 mAh g^{-1}	[17]
$Li_3V_{1.98}Fe_{0.02}(PO_4)_3$	3.0-4.9 V	0.2 C	177 mAh g^{-1}	[18]
$Li_3V_{1.9}Cr_{0.1}(PO_4)_3$	3.0-4.8 V	0.2 C	171 mAh g^{-1}	[19]
$Li_3V_{1.95}Sn_{0.05}(PO_4)_3$	2.5-4.5 V	0.5 C	136 mAh g^{-1}	[20]
$Li_3V_{1.8}Mg_{0.3}(PO_4)_3$	3.0-4.3 V	1 C	127 mAh g^{-1}	[21]
$Li_3V_{1.85}Sc_{0.15}(PO_4)_3$	3.0-4.8 V	5 C	87 mAh g^{-1}	[11]
$Li_3V_{1.9}Co_{0.1}(PO_4)_3$	3.0-4.8 V	10 C	115 mAh g^{-1}	[22]

2.2. Experimental

The pristine $Li_3V_2(PO_4)_3$ electrode active material was synthesized via a spray-drying-assisted carbothermal reaction. A stoichiometric mixture of the starting materials, $LiOH{\cdot}H_2O$ (Sigma-Aldrich), NH_4VO_3 (Wako), and $NH_4H_2PO_4$ (Wako), was dissolved in 200 ml of water and stirred with a rotating speed of 300 rpm at 80 °C for 1 h. Citric acid (10% by weight), which acts as not only a chelating agent but also is a reductive agent, was further added, and then the solution was kept at 120 °C for 1 h under magnetic stirring. In order to prepare homogeneous precursors for a spray-drying-assisted carbothermal reaction, the pH of the solution was fixed between 9 and 12. The solution was spray-dried at a rate of 10 mL min^{-1} with an inlet temperature of 220 °C and an outlet temperature of 110 °C and further pre-heated at 300 °C for 5 h. The resulting powder was pelletized, heated at 700 °C for 10 h in an argon atmosphere, and cooled to room temperature at a rate of 100 °C/h. The procedures for Al- and Fe-doped $Li_3V_2(PO_4)_3$ were the same except for the addition of the stoichiometric ratio of $Al(NO_3)_3{\cdot}9H_2O$ and $FeC_2O_4{\cdot}2H_2O$ (Sigma-Aldrich), respectively.

The crystalline $Li_{1.5}Al_{0.5}Ge_{1.5}(PO_4)_3$ solid-state electrolyte was synthesized using stoichiometric ratios of the starting materials, Li_2CO_3, GeO_2 (Shinko Chemical), $NH_4H_2PO_4$, and Al_2O_3 (Nippon Light Metal). The mixture was heated at 500 °C for 2 h and ground. It was then heated to 800 °C for 6 h and further sintered at 900 °C

for 2 h in the air. This material had well-developed XRD reflections showing it is well-crystallized. Amorphous $Li_{1.5}Al_{0.5}Ge_{1.5}(PO_4)_3$ was also prepared by quenching melted $Li_{1.5}Al_{0.5}Ge_{1.5}(PO_4)_3$ (1200 °C) in iced water.

X-ray diffraction patterns of the samples were obtained by an X-ray diffractometer (XRD, RINT-2500 TTR-III, Rigaku; Cu-Kα, 50 kV, 300 mA) in 2Θ range of 10-80° at a scan rate of 0.1°/min with a step of 0.02° and refined by the Fullprof Suite refinement program using atomic coordinates of monoclinic $Li_3V_2(PO_4)_3$ single crystal data [23]. The working electrodes were prepared by ball-milling a mixture of 70 wt.% active materials and 25 wt.% acetylene black. 5 wt.% PTFE binder was then added. Pellets with approximate weight of 30 mg were prepared manually using a mortar and a pestle. The electrode materials in 2032 coin cells were assembled with 1 M $LiPF_6$ in EC : DMC (1:1 by volume) as the electrolyte. The charge and discharge performances of the material used as a cathode, and as an anode vs. Li (half cell) and the full symmetric cell were evaluated at a current rate of 7.5 mA g^{-1} in the voltage ranges of 3.0-4.5 V (cathode), 3.0-1.5 V (anode), and 0.0-3.0V (full symmetric cell), respectively.

The crystalline $Li_{1.5}Al_{0.5}Ge_{1.5}(PO_4)_3$ was pressed at 20 MPa into a pellet and heated at 840 °C for 2 h to prepare a NASICON-type solid-state electrolyte. The working electrodes for all-solid-state symmetric cells were prepared using a mixture of electrode active materials (49 wt.%), amorphous $Li_{1.5}Al_{0.5}Ge_{1.5}(PO_4)_3$ (49 wt.%), and

vapor-grown carbon fiber (VGCF, Showa Denko; 2 wt.%). This mixture (97 wt.%) was then mixed with BL-S polyvinyl alkyl acetyl alcohol (BL-S, Sekisui Chemical Co.; 3 wt.%) and 2,2,4-trimethyl-2,4-pentanediol monoisobutyrate (CS-12, Chisso Corp.) to make a paste. This paste was screen-printed on both sides of the $Li_{1.5}Al_{0.5}Ge_{1.5}(PO_4)_3$ pellets. The resulting 0.7 mm pellets were hot-pressed to final thickness of 0.6 mm at 600 °C for 2 h in Ar atmosphere and Pt-coated for the measurements.

The charge and discharge performances of all-solid-state symmetric cells were examined at a current rate of 7.5 mA g^{-1} in a voltage range of 0.0-3.0 V at room temperature. In addition, the morphology of the pristine and cation-doped $Li_3V_2(PO_4)_3$ samples and cross-sectional images of $Li_{1.5}Al_{0.5}Ge_{1.5}(PO_4)_3$ pellets were recorded by scanning electron microscopy (SEM). The electrical conductivity of the samples was evaluated using powder resistivity measuring system (Mitsubishi Chemical Analytech, Japan). The resistivity measuring system is equipped with high precision pressure gauge directly attached to a teflon-coated cylindrical holder (model MCP-PD522), allowing measurements under various pressures taking into account the sample thickness, its volume and density under given pressure. Measured volume resistivities are calculated in accordance with the equation:

$$\rho_v[\Omega\ \text{cm}] = R[\Omega] \times RCF \times t[\text{cm}] \qquad (2.6)$$

where ρ_v is the volume resistivity, R is resistance measured by applying Ohm's law, *RCF* is Resistivity Correction Factor, and t is sample thickness.

The machine is equipped with analysis software which finds resistivity correction factors automatically. The measurement of a powder sample is achieved by pressing the pellet of the measured powder under various predefined forces, the maximum being 20 kN corresponding to ca. 60 MPa for the MCP-PD522 cell geometry. Resistance versus press power plot is automatically generated and the conductivity is calculated as the inverse of the volume resistance. Further details can be obtained by Mitsubishi Chemical Analytech.

2.3. Results and Discussion

The structural modification of isotypic structures from monoclinic to orthorhombic systems has reportedly been induced by introducing mixed-metallic systems, $Li_2TiM(PO_4)_3$ (M = Fe, Cr) [24], $Li_{3-2x}(Sc_{1-x}M_x)_2(PO_4)_3$ (M = Ti, Zr, Sn, Hf) [25], and $Li_{3-2x}(V_{1-x}Zr_x)_2(PO_4)_3$ ($x \geq 0.05$) [26].

However, the powder diffraction patterns of the Al- and Fe-doped $Li_3V_2(PO_4)_3$ were identified not as *Pbcn* or *Pbca* orthorhombic, but as $P2_1/c$ monoclinic phases (**Fig. 2-2**). The background of XRD profile was fitted with linear interpolation between a set of 82 points with refinable heights, and the peak shape was

refined with the convolution of a pseudo-Voigt function. The atomic fractional coordinates obtained from single crystal data were adopted for the refined structures.

To treat negative atomic displacement parameters of the pristine $Li_3V_2(PO_4)_3$ sample that may be attributable to the obtained bulky spray-dried powders, atomic distance restraints and absorption parameters were introduced. The refinements were carried out simultaneously until satisfactory *R*-factors were obtained (R_{wp} = 6.47%, R_B = 3.48% for pristine $Li_3V_2(PO_4)_3$, R_{wp} = 4.97%, R_B = 1.66% for $Li_3V_{1.9}Fe_{0.1}(PO_4)_3$, and R_{wp} = 3.33%, R_B = 1.81% for $Li_3V_{1.9}Al_{0.1}(PO_4)_3$), as illustrated in **Fig. 2-3**. The calculated unit cell volume values are as follows: $Li_3V_2(PO_4)_3$ (V = 887.73 $Å^3$), Fe-doped $Li_3V_2(PO_4)_3$ (V = 888.27 $Å^3$) and Al-doped $Li_3V_2(PO_4)_3$ (V = 885.41 $Å^3$), which were in good

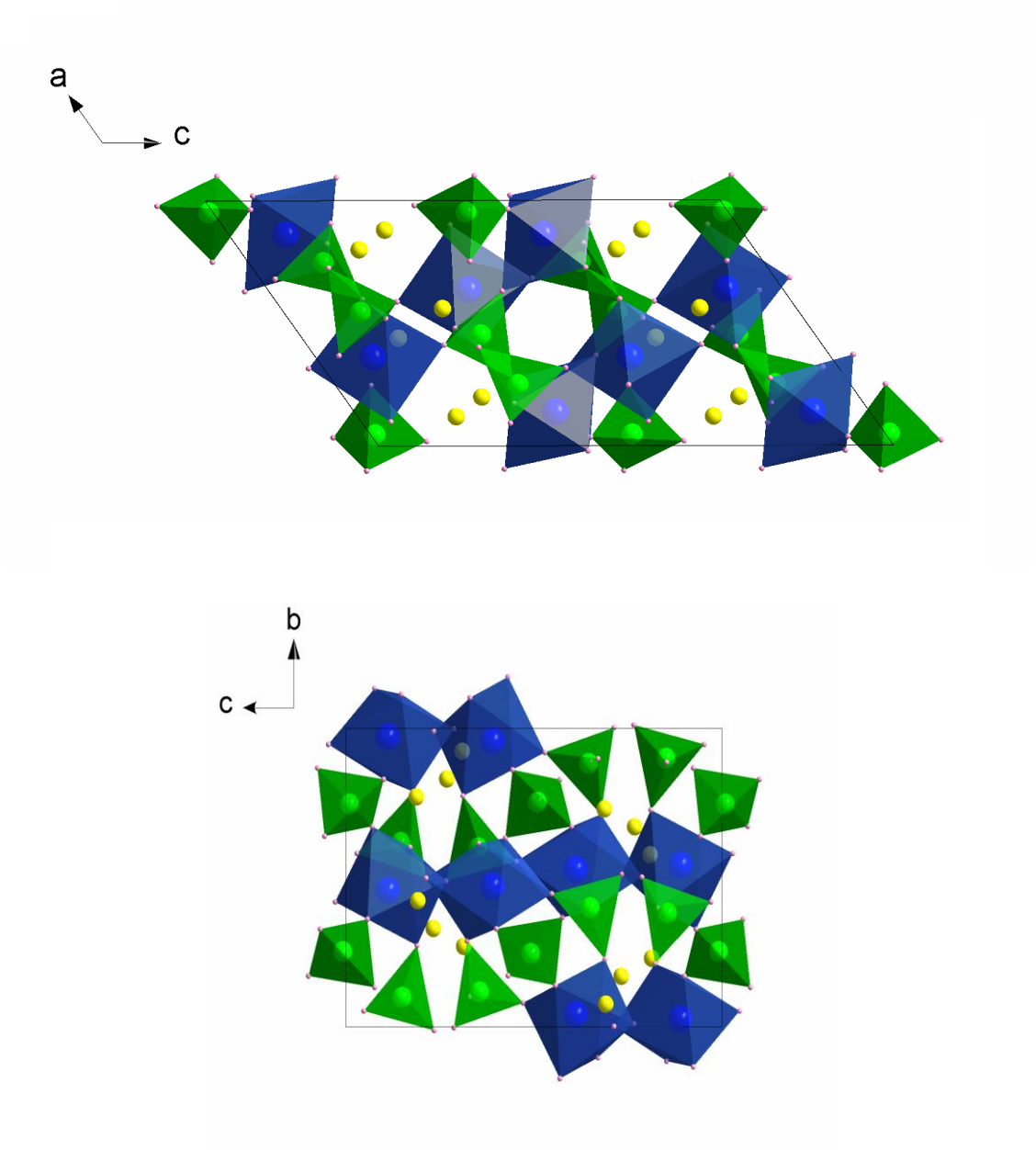

Fig. 2-2 Schematic view of the monoclinic $Li_3V_2(PO_4)_3$ (*$P2_1/c$*, #14) comprised of PO_4 tetrahedra (green) and VO_6 octahedra (blue) along the b-axis and the a-axis.

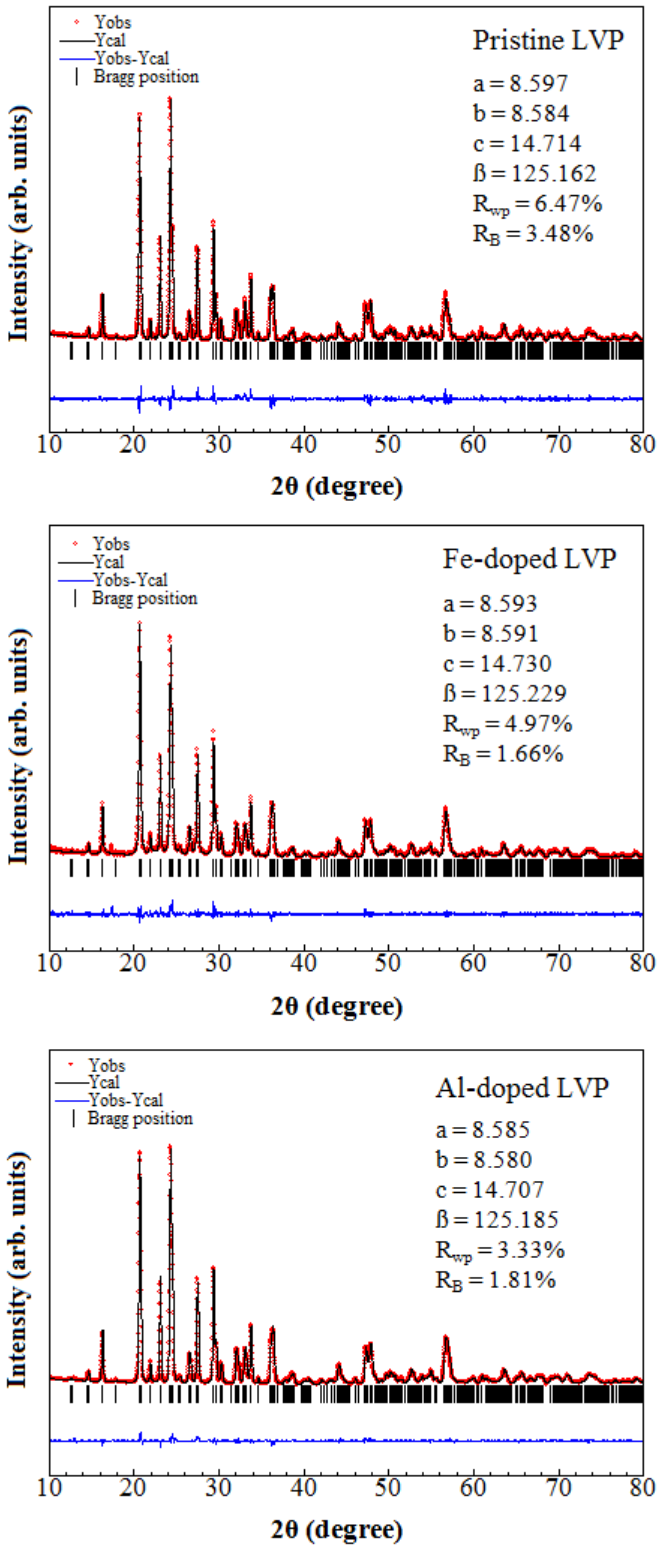

Fig. 2-3 Powder diffraction profiles of the observed (circles) and calculated (solid lines) patterns for pristine $Li_3V_2(PO_4)_3$, Fe-doped $Li_3V_2(PO_4)_3$, and Al-doped $Li_3V_2(PO_4)_3$.

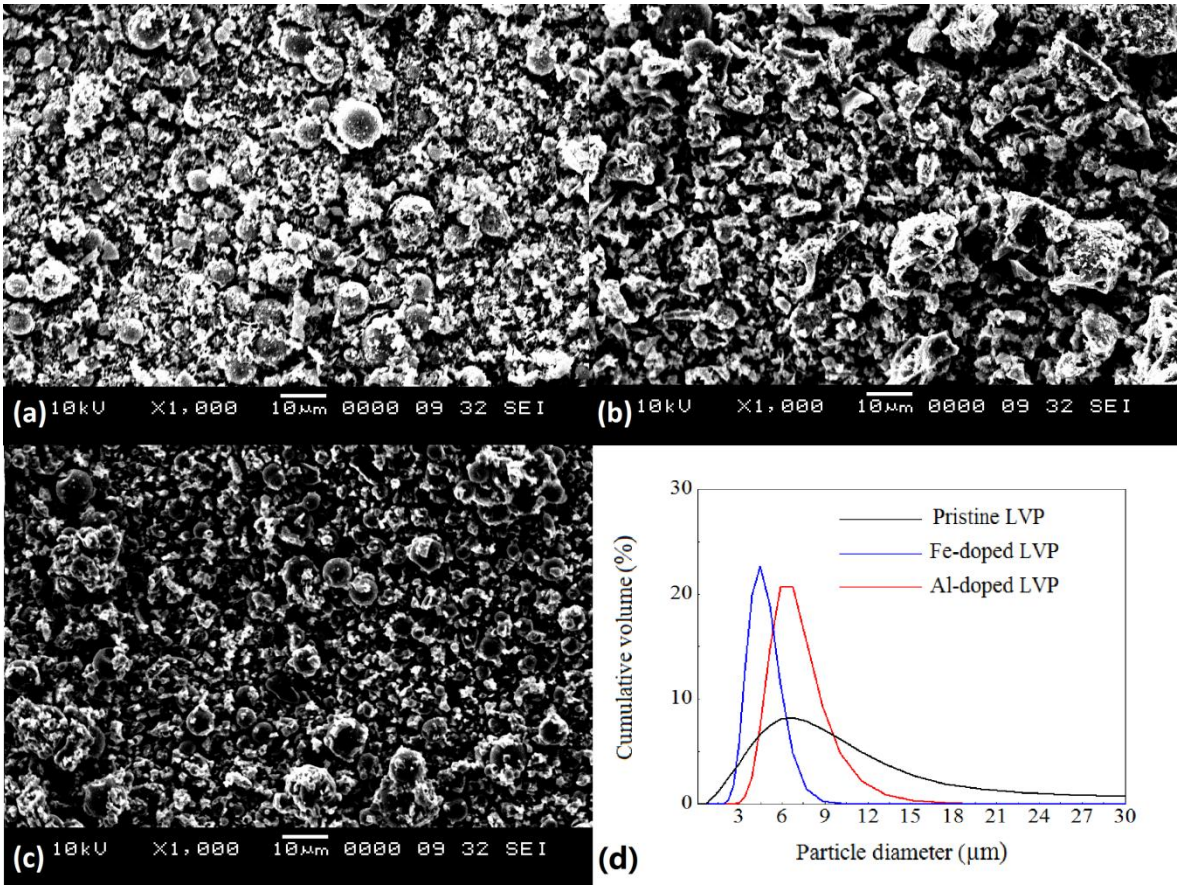

Fig. 2-4 SEM images of pristine $Li_3V_2(PO_4)_3$ (a), Fe-doped $Li_3V_2(PO_4)_3$ (b), Al-doped $Li_3V_2(PO_4)_3$ (c), and their particle-size distribution curves (d). The measurements were carried out after the carbothermal synthesis.

agreement with crystal radius of the dopants. Bond-valence-sum calculations were in good agreement with classical valence of +III for V, Al, and Fe. The difference Fourier map indicated that possible Li sites other than the three initially assigned independent sites were located either on negative levels or relatively too close to both O and M atoms, which were barely allowed at the maximum occupancy of less than 20% of Li ions. Therefore, initial Li sites with full occupancies were adopted for the refinement. SEM images of pristine $Li_3V_2(PO_4)_3$, $Li_3V_{1.9}Al_{0.1}(PO_4)_3$, and $Li_3V_{1.9}Fe_{0.1}(PO_4)_3$ are shown in **Fig. 2-4**. All prepared samples are composed of spherical particles, ranging from 0.1 μm to 30 μm in diameter, but were not as homogeneous as previously reported spray-dried $Li_3V_2(PO_4)_3$ [27]. This could be attributed to particle agglomeration and destruction of relatively soft spherical particles of the spray-dried precursor, caused by the pelletizing performed prior the carbothermal reduction process. The initial charge and discharge performances of $Li_3V_2(PO_4)_3$, $Li_3V_{1.9}Al_{0.1}(PO_4)_3$, and $Li_3V_{1.9}Fe_{0.1}(PO_4)_3$ electrodes against Li are shown in **Fig. 2-5**.

The cathode and anode performances were measured at a current rate of 7.5 mA g^{-1} in the range of 3.0-4.5 V as cathode and 3.0-1.5 V as anode, respectively. The initial capacities of undoped $Li_3V_2(PO_4)_3$ were 112.4 mAh g^{-1} (3.0 V -> 4.5 V, charging) and 122.7 mAh g^{-1} (3.0 V -> 1.5 V, discharging), respectively. On the other hand, these capacities were improved more than 10 % by cation doping as follows; 123.8 mAh g^{-1} (3.0 V -> 4.5 V) and 132 mAh g^{-1} (3.0 V -> 1.5 V) for $Li_3V_{1.9}Al_{0.1}(PO_4)_3$, and

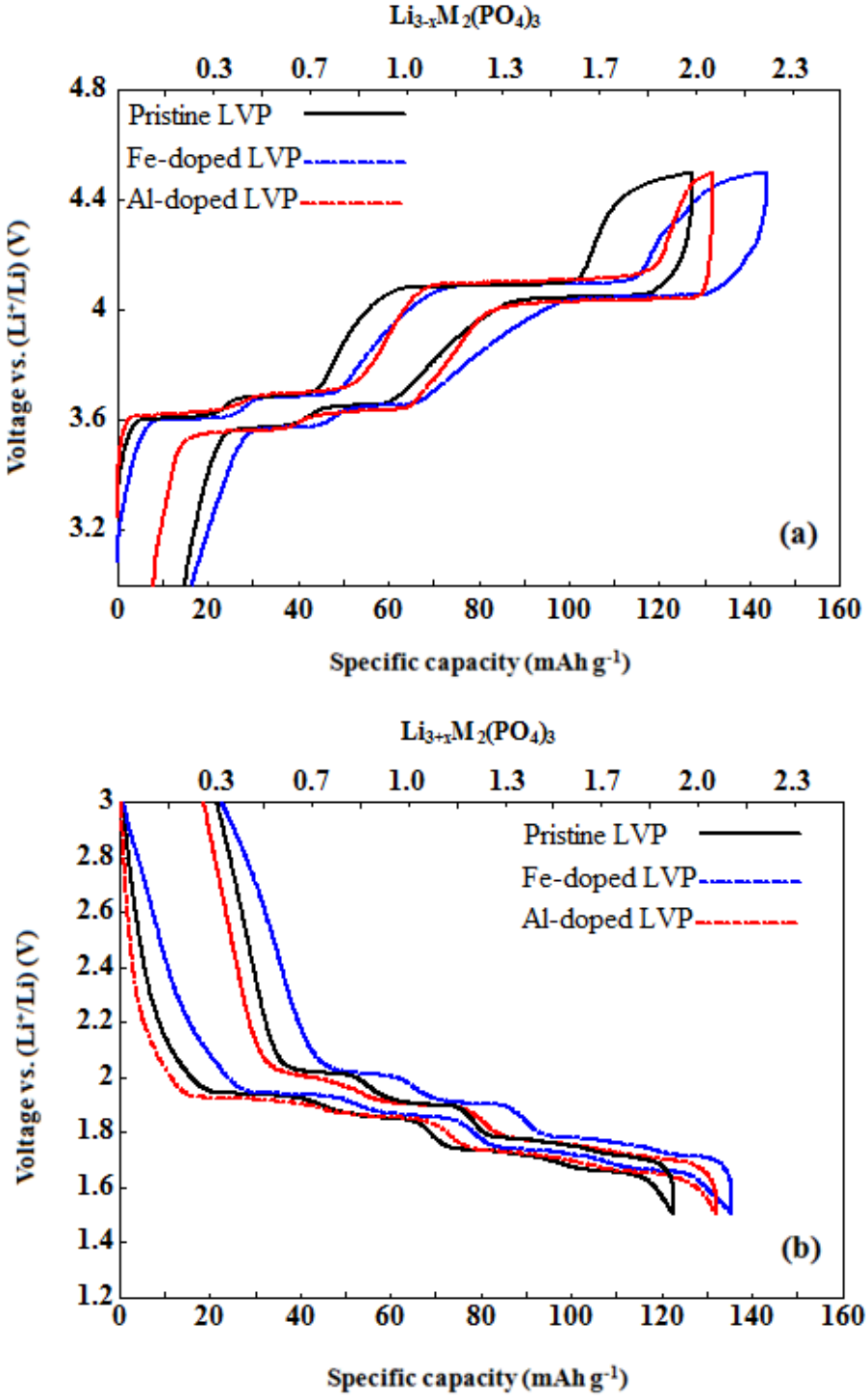

Fig. 2-5 The initial charge and discharge curves of pristine $Li_3V_2(PO_4)_3$, Fe-doped $Li_3V_2(PO_4)_3$, and Al-doped $Li_3V_2(PO_4)_3$ at a current rate of 7.5 mA g^{-1} in the voltage ranges of (a) 3.0-4.5 V and (b) 3.0-1.5 V.

Table 2-6. The electrical conductivity of the $Li_3V_2(PO_4)_3$, and its Al-, and Fe-doped derivatives.

	$\mathbf{Li_3V_2(PO_4)_3}$	$\mathbf{Li_3V_{1.9}Al_{0.1}(PO_4)_3}$	$\mathbf{Li_3V_{1.9}Fe_{0.1}(PO_4)_3}$
σ (S cm^{-1})	1.86×10^{-6}	5.35×10^{-5}	4.12×10^{-5}

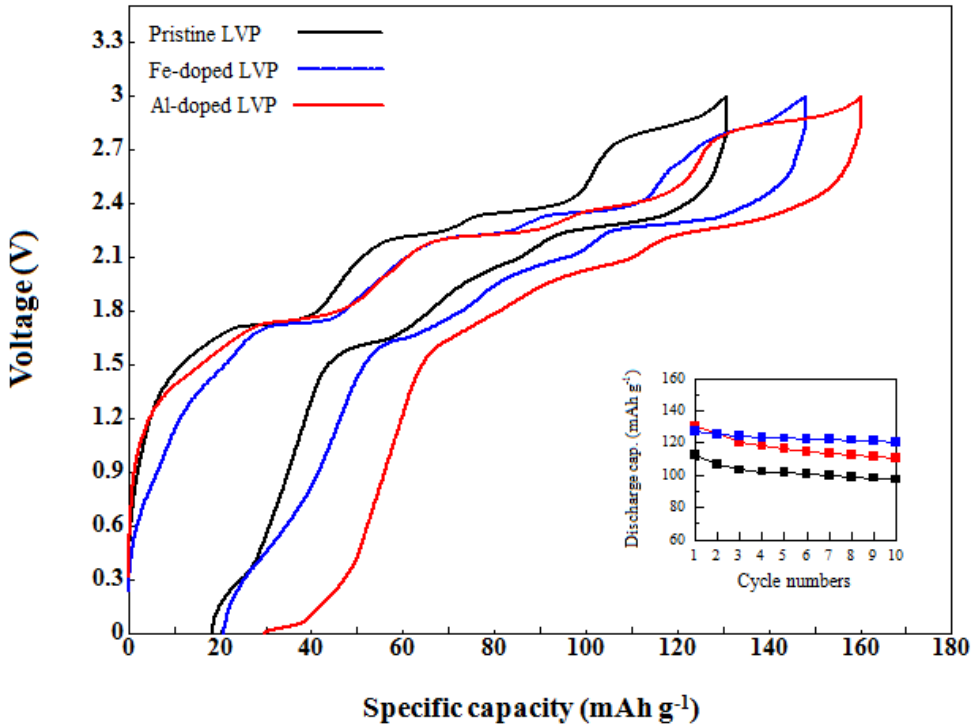

Fig. 2-6 The initial charge and discharge curves of pristine $Li_3V_2(PO_4)_3$, Fe-doped $Li_3V_2(PO_4)_3$, and Al-doped $Li_3V_2(PO_4)_3$ symmetric cells at a current rate of 7.5 mA g^{-1} in a voltage range of 0.0-3.0 V with 1 M $LiPF_6$ in EC : DMC (1:1 in volume) as electrolyte. Cycle life is shown in the inset.

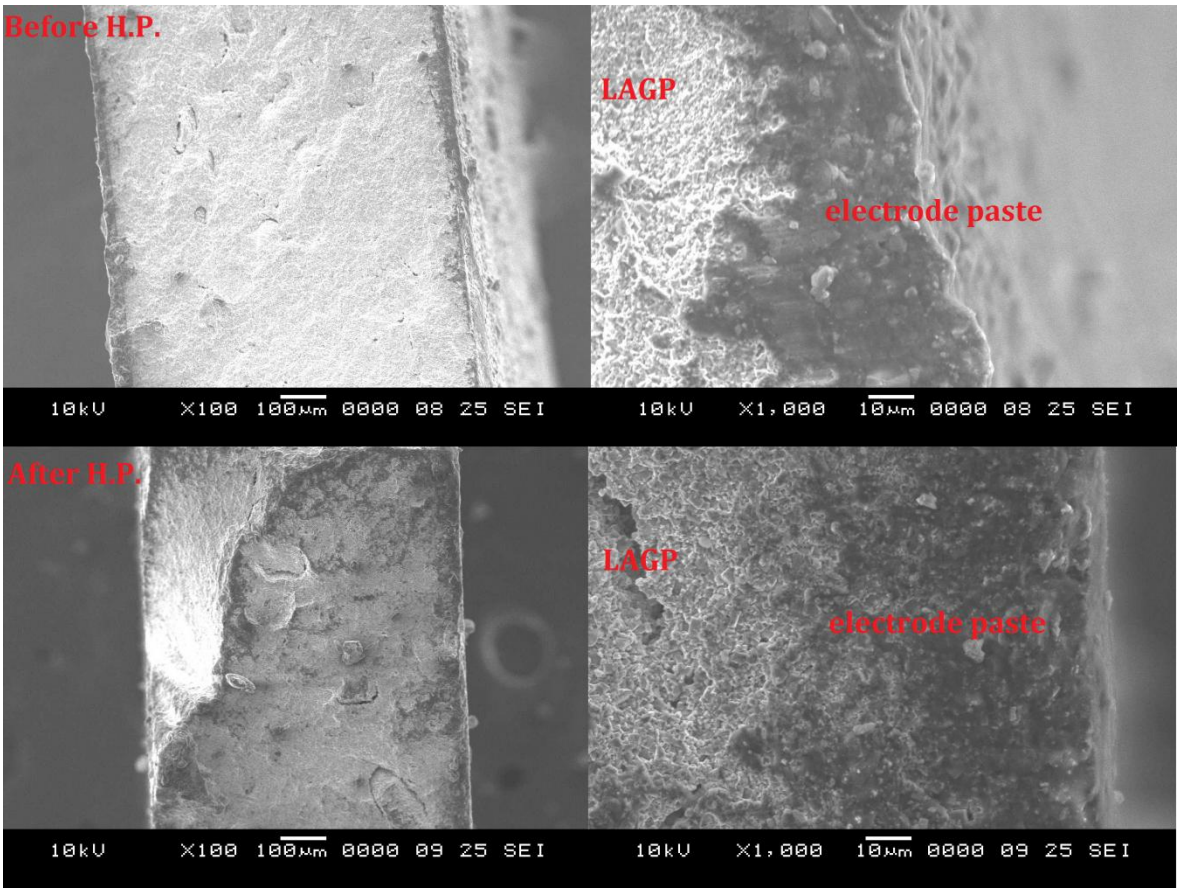

Fig. 2-7 Cross-sectional SEM images of all-solid-state symmetric cell pellet before (upper left) and after (bottom left) hot-pressing process.

127.2 mAh g^{-1} (3.0 V -> 4.5 V) and 135.6 mAh g^{-1} (3.0 V -> 1.5V) for $Li_3V_{1.9}Fe_{0.1}(PO_4)_3$, respectively. The increased specific capacities of Al- and Fe-doped $Li_3V_{1.9}M_{0.1}(PO_4)_3$ could be attributed to the increased electronic conductivity listed in **Table 2-6**. *dQ*/*dV* plots of these electrodes are in good agreement with previously reported data [11], having three and four plateaus in the potential window of 3.0 - 4.5 V (cathode side) and 3.0 - 1.5 V (anode side) during the charge and discharge reactions. However, no observable peaks for Fe^{2+}/Fe^{3+} and Fe^{3+}/Fe^{4+} were found on either profile. It means that heterogeneous incorporation of the iron phosphate phase did not occur in spray-dried monoclinic $Li_3V_{2-x}Fe_x(PO_4)_3$ [28] when $x < 0.1$.

Fig. 2-6 shows the charge/discharge performance of liquid electrolyte symmetric cells with $Li_3V_2(PO_4)_3$, $Li_3V_{1.9}Al_{0.1}(PO_4)_3$, and $Li_3V_{1.9}Fe_{0.1}(PO_4)_3$ electrodes (cathode/anode weight balance 1:1) in the voltage range of 0-3.0 V at a current rate of 7.5 mA g^{-1}. The initial discharge capacity for $Li_3V_2(PO_4)_3$, $Li_3V_{1.9}Al_{0.1}(PO_4)_3$, and $Li_3V_{1.9}Fe_{0.1}(PO_4)_3$ symmetric cells were 112.5 mAh g^{-1}, 130.4 mAh g^{-1}, and 127.2 mAh g^{-1}, respectively. Al-doped $Li_3V_2(PO_4)_3$ at a current rate of 7.5 mA g^{-1} in the voltage ranges of (a) 3.0-4.5 V and (b) 3.0-1.5 V. The same materials were tested in all-solid-state configuration with amorphous $Li_{1.5}Al_{0.5}Ge_{1.5}(PO_4)_3$ electrolyte as explained in the experimental section. Cross-sectional SEM images of the all-solid state cells are shown in **Fig. 2-7**. The initial all-solid-state pellet with an average thickness of

ca. 0.8 mm is reduced to ca. 0.6 mm after the hot-pressing process. These hot-pressed all-solid-state symmetric cells exhibited the following initial discharge capacities: 103.3 mAh g^{-1} for $Li_3V_2(PO_4)_3$, 107.6 mAh g^{-1} for Fe-doped $Li_3V_2(PO_4)_3$, and 105.6 mAh g^{-1} for Al-doped $Li_3V_2(PO_4)_3$. However, it is clearly seen in **Fig. 2-8** that even at this low current density (7.5 mA g^{-1}), the all-solid state cells suffer from large polarization with continuous capacity fade.

The specific conductivity of the $Li_{1.5}Al_{0.5}Ge_{1.5}(PO_4)_3$ has been known as ca. 2.4 x 10^{-4} S cm^{-1} [29], and its specific resistance is therefore 4166 Ω cm. Since the thickness of the pellet is 0.6 mm (0.06 cm), the resistance due to the $Li_{1.5}Al_{0.5}Ge_{1.5}(PO_4)_3$ pellet is 4166 Ω cm x 0.06 cm ~ 250 Ω cm^2. When the low current density of 10 μA cm^{-2} (~ 7.5 mA g^{-1}) is applied, polarization due to the bulk resistance of the $Li_{1.5}Al_{0.5}Ge_{1.5}(PO_4)_3$ pellet is calculated to be only

$$1.0\text{x } 10^{-5} \text{ A cm}^{-2} \text{ x } 250 \text{ Ω cm}^2 \sim 0.0025 \text{ V} \qquad (2.7)$$

Despite this low theoretical value, the all-solid-state symmetric cells showed significantly large polarization, which could be attributed to huge interfacial resistance between electrodes and solid-state electrolyte. As interfacial resistance is one of the key aspects in the all-solid-state batteries further study is necessary to deal with it. A possible approach would be to use alternative solid film formation technique such as

pulsed laser deposition (PLD), which is capable to deposit very thin and uniform films on the surface of the electrodes. Alternatively, other solid-state electrolytes with lower intergrain resistance (e.g. sulphides, borohydrides, garnets, etc.) could be studied. However, the compatibility between any given solid-state electrolyte and any particular electrode material should be verified, which is a very broad field for further exploration.

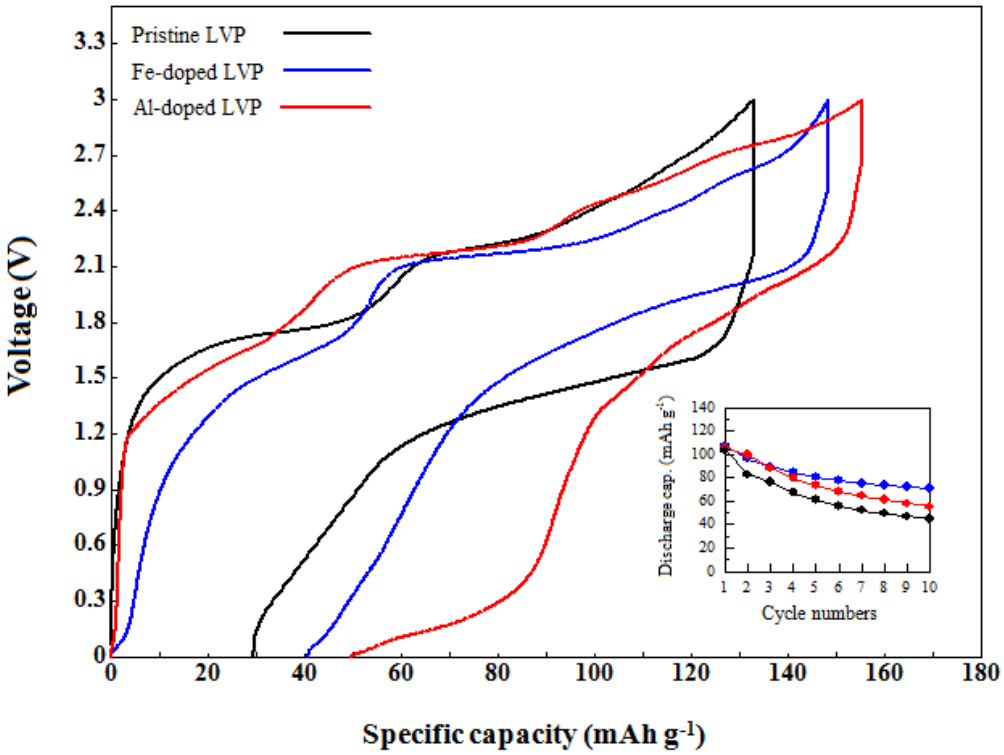

Fig. 2-8 The initial charge and discharge curves of pristine $Li_3V_2(PO_4)_3$, Fe-doped $Li_3V_2(PO_4)_3$, and Al-doped $Li_3V_2(PO_4)_3$ all-solid-state symmetric cells at a current rate of 7.5 mA g^{-1} in the voltage range of 0.0-3.0 V with $Li_{1.5}Al_{0.5}Ge_{1.5}(PO_4)_3$ solid-state electrolyte. Cycle life is shown in the inset.

References

[1] M. Park, X. Zhang, M. Chung, G. B. Less, and A. Sastry, *J. Power Sources,* **195** (2010) 7904.

[2] P. Han, Y. Zhu, and J. Liu, *J. Power Sources*, **284** (2015) 459.

[3] Y. Inda, T. Katoh, and M. Baba, *J. Power Sources,* **174** (2007) 741.

[4] A. Sakuda, H. Kitaura, A. Hayashi, M. Tatsumisago, Y. Hosoda, T. Nagakane, and A. Sakamoto, *Chem Lett.,* **41** (2012) 260.

[5] E. Kobayashi, A. Kitajou, S. Okada, and J. Yamaki, *J. Power Sources,* **244** (2013) 312.

[6] H. Kitaura, A. Hayashi, K. Tadanaga, and M. Tatsumisago, *J. Electrochem. Soc.*, **157** (2010) A407.

[7] J. F. Shackelford. Introduction To Materials Science FOR ENGINEERS. Ed. by Dept. of Materials Science and Engineering. University of Tennessee, 1975, Ch. 19.

[8] M. A. Green, *J. Appl. Phys.*, **67** (1990) 2944.

[9] X. Rui, Q. Yan, M. Skyllas-Kazacos, and T. Lim, *J. Power Sources,* **258** (2014) 19.

[10] X. Zhang, S. Q. Liu, K.L. Huang, S. X. Zhuang, J. Guo, T. Wu, and P. Cheng, *J. Solid State Electrochem.*, **163** (2012) 937.

[11] C. W. Sun, S. Rajasekhara, Y. Z. Dong, and J. B. Goodenough, *ACS Appl. Mater. Interfaces,* **3** (2011) 3772.

[12] X. P. Zhang, H. J. Guo, X. H. Li, Z. X. Wang, and L. Wu, *Electrochim. Acta,* **64**

(2012) 65.

[13] M. M. Ren, Z. Zhou, X. P. Gao, W. X. Peng, and J. P. Wei, *J. Phys. Chem., C* **112** (2008) 5689.

[14] A. Q. Pan, D. W. Choi, J. G. Zhang, S. Q. Liang, G. Z. Cao, Z. M. Nie, B. W. Arey, and J. Liu, *J. Power Sources*, **196** (2011) 3646.

[15] L. J. Wang, Z. Y. Tang, L. Ma, and X. H. Zhang, *Electrochem. Commun.*, **13** (2011) 1233.

[16] Y. Q. Qiao, J. P. Tu, J. Y. Xiang, X. L. Wang, Y. J. Mai, D. Zhang, and W. L. Liu, *Electrochim. Acta*, **56** (2011) 4139.

[17] A. R. Cho, J. N. Son, V. Aravindan, H. Kim, K. S. Kang, W. S. Yoon, W. S. Kim, and Y. S. Lee, *J. Mater. Chem.*, **22** (2012) 6556.

[18] M. M. Ren, Z. Zhou, Y. Z. Li, X. P. Gao, and J. Yan, *J. Power Sources*, **162** (2006) 1357.

[19] Y. H. Chen, Y. M. Zhao, X. N. An, J. M. Liu, Y. Z. Dong, and L. Chen, *Electrochim. Acta*, **54** (2009) 5844.

[20] H. P. Liu, S. F. Bi, G. W. Wen, X. G. Teng, P. Gao, Z. J. Ni, Y. M. Zhu, and F. Zhang, *J. Alloys Compd.*, **543** (2012) 99.

[21] J. S. Huang, L. Yang, K. Y. Liu, and Y. F. Tang, *J. Power Sources*, **195** (2010) 5013.

[22] K. Nathiya, D. B. Gangulibabu, D. Nirmala, and N. Kalaiselvi, *RSC Adv.*, **2** (2012)

6885.

[23] Y. Kee and H. Yun, *Acta Cryst., E***69** (2013) i11.

[24] S. Patoux, G. Rousse, J. -B. Leriche, and C. Masquelier, *Solid State Sciences*, **6** (2004) 1113.

[25] T. Suzuki, K. Yoshida, K. Uematsu, T. Kodama, K. Toda, Z. Ye, and M. Sato, *Solid State Ionics*, **104** (1997) 27.

[26] M. Sato, H. Ohkawa, K. Yoshida, M. Saito, K. Uematsu, and K. Toda, *Solid State Ionics*, **135** (2000) 137.

[27] L. -L. Zhang, G. Peng, G. Liang, P. -C. Zhang, Z. -H. Wang, Y. Jiang, Y. -H. Huang, and H. Lin, *Electrochim. Acta*, **90** (2013) 433.

[28] L. -L. Zhang, G. Liang, G. Peng, Y. -H. Huang, L. Wang, L. Qie, M. C. Croft, A. Ignatov, and J. B. Goodenough, *J. Electrochem. Soc*., **159** (2012) A1573.

[29] H. Aono, E. Sugimoto, Y. Sadaoka, N. Imanaka, and G. Adachi, *Bull. Chem. Jpn*., **65** (1992) 2200.

CHAPTER 3

Orthorhombic Lithium Titanium Phosphate as an Anode Material for Li-ion Rechargeable Battery

3. 1. Introduction

There has been increasing interests on non-conventional set of batteries including aqueous Li-ion rechargeable battery. This type of battery has been rooted from traditional galvanic cell, which mainly uses cheap water as solvent for Li-salt. The advantage of aqueous Li-ion cell over conventional galvanic or metal hydride cell does not only come from removal of memory effect, but also use of non-organic electrolyte. Solid State Interface (SEI) formation, which is known to protect electrode components, is also a major reason for capacity loss in long cycle and SEI formation rate could be represented as follows [1]:

$$s = \frac{\sqrt{2c\rho mk^2Dt + D^2\rho^2} - D\rho}{\rho k} \tag{3.1}$$

$$s = \frac{\sqrt{2cmDt}}{\rho} - \frac{D}{k} \text{ (when large t is limited)} \tag{3.2}$$

$$\Delta c = \frac{Js}{AD}, J = kA(c - \Delta c) \tag{3.3}$$

where m is mass of SEI formed by a single reaction, ρ is density of SEI, A is surface of anode (graphite), D is the diffusivity of the species that reacts with Li through SEI, c is the concentration of the species, and k is reaction rate constant. Also, capacity fade,

which is originated from changes in current and overpotential by SEI could reportedly be described as [1, 2]:

$$J_{\mathrm{SEI}} = 2\mathrm{i}_{\mathrm{SEI}}\sinh\left(\frac{-e\mu_{\mathrm{SEI}}}{2k_{\mathrm{B}}T}\right) \quad (3.4)$$

$$\mu_{\mathrm{SEI}} = \varphi_{\mathrm{electrode}} - \varphi_{\mathrm{electrolyte}} - \Delta\varphi_{\mathrm{SEI}} + JR \quad (3.5)$$

where φ is potential, $\Delta\varphi_{\mathrm{SEI}}$ is equilibrium potential for SEI formation, and i_{SEI} is exchange current density depending on Li-ion and electrolyte molecule in the presence of SEI.

However, aqueous rechargeable Li-ion battery could replace current organic electrolytes by using aqueous electrolyte, which could also considerably reduce the production cost of the lithium-ion batteries and completely eliminate the fire hazard at the expense of reduced energy density. On the other hand, the voltage window of the aqueous electrolytes should be strictly controlled to prevent electrolysis of water, represented by following half-cell reactions:

Oxidation at the anode:

$$2\ H_2O\ (l) \rightarrow O_2\ (g) + 4H^+\ (aq) + 4e^-\ (E^o_{ox} = -1.23\ V) \qquad (3.6)$$

$$E_{O_2(g)/H_2O(l)} = E^o_{O_2(g)/H_2O(l)} + \frac{RT}{nF} \ln(P_{O_2(g)}[H^+]^4) \qquad (3.7)$$

Reduction at the cathode:

$$2H^+\ (aq) + 2e^- \rightarrow H_2\ (g)\ (E^o_{red} = 0.0\ V) \qquad (3.8)$$

$$E_{H_2(g)/H^+} = E^o_{H_2(g)/H^+} - \frac{RT}{nF} \ln(\frac{P_{H_2}}{[H^+]^2}) \qquad (3.9)$$

Therefore, the standard potential of water electrolysis is -1.23 V at standard conditions (25 ^oC and 101 kPa). According to the Nernst equation, this standard potential values mean generation of H_2 and O_2 occurs at approximately 2.6 V and 3.8 V, respectively vs. Li at pH 7, which allows only non-conventional sets of anode electrode materials to meet the proper working voltage of ~1.2 V in the full-cell configuration [3]. One of the most well-known and proper anode materials is NASICON-type $LiTi_2(PO_4)_3$ with theoretical capacity of 138 mAh g^{-1} and redox potential of 2.5 V for Ti^{3+}/Ti^{4+} couple. **Table 3-1** lists previously reported possible aqueous Li-ion rechargeable batteries along with $LiTi_2(PO_4)_3$–based aqueous cells. In general, non-carbonaceous

anode material such as $LiTi_2(PO_4)_3$ has advantage on cycle life compare to conventional carbonaceous anode because there is no capacity loss from Solid Electrolyte Interphase (SEI).

However, regardless of the nature of the cathode materials, comparably large irreversibility has been systematically observed, followed by gradual capacity fading of full aqueous Lithium-ion cells with $LiTi_2(PO_4)_3$ anodes. This electrochemical behavior has hindered its application as an anode for aqueous Li-ion batteries. The reason for this is not clear. However, one of the major reasons could be attributed to the generation of electrochemically inactive phase $Li_{3+0.5y}Ti_2(PO_4)_3$ (y = small amount of extra lithium) with lowered *R-3* symmetry, which is reported on ICSD database, during the repetitive Li-insertion processes. In such case, the net reaction can be represented in the following manner:

Li-insertion:

$$LiTi_2(PO_4)_3 + 2Li^+ + 2e^- \rightarrow (1\text{-}z)Li_3Ti_2(PO_4)_3 + z[Li_{3-0.5y}Ti_2(PO_4)_3/Li_{3+0.5y}Ti_2(PO_4)_3];\ z \sim 0 \quad (3.10)$$

Li-extraction:

$(1\text{-}z)Li_3Ti_2(PO_4)_3 + (0.5z)Li_{3\text{-}0.5y}Ti_2(PO_4)_3 \rightarrow LiTi_2(PO_4)_3 + (2\text{-}0.5z)Li^+ + (2\text{-}0.5z)e^-$

(3.11)

In such case, the phase transitions could be explained by one in follows:

- nucleation-and-growth transitions
- order-disorder transitions
- martensitic transitions

In nucleation-and-growth transitions, new phases with specific critical sizes need to be first formed in the parent phase and the change in free energy, ΔG due to formation of spherical nuclei could be represented by:

$$\Delta G = -4/3\pi r^3 \Delta G_v + 4\pi r^2 \gamma \qquad (3.12)$$

where $-4/3\pi r^3 \Delta G_v$ represents the decrease in bulk free energy and $4\pi r^2 \gamma$ represents increase in surface free energy.

Table 3-1. Previously reported aqueous rechargeable Li-ion batteries.

Cathode	**Anode**	**Electrolyte**	**Initial capacity ($mAh\ g^{-1}$)**	**Ref**
Li_2MnO_4	$LiTi_2(PO_4)_3$	1 M Li_2SO_4	57.56	[4]
$LiFePO_4$	$LiTi_2(PO_4)_3$	Saturated Li_2SO_4	87	[5]
$Li(Ni/Co/Mn)O_2$	LiV_3O_8	Saturated Li_2SO_4	95.2	[6]
$LiCoO_2$	Li_2MnO_4	5 M $LiNO_3$	105	[3]
$LiFePO_4$	VO_2	Saturated $LiNO_3$	106	[7]

If spherical nucleus, *r*, is small enough, the increase in surface free energy will dominate the free energy and the phase transition will be thermodynamically unfavorable, while nucleus reaches its critical radius, the free energy will begin to decrease, which will make this phase transition thermodynamically favorable. The order-disorder transitions are rather common in electrode host materials, because they are associated with positional disordering, orientational disordering, or electronic spin-sates disordering and their corresponding entropy could be represented as following equation:

$$\Delta S = R \ln (A/B) \qquad (3.13)$$

where *A* and *B* are total number of configurations or orientations in the product and parent phase, respectively. The martensitic transition is structurally induced by destructive homogeneous atomic displacements, which result in invariant plane between product and parent phases. Meanwhile, there could be two phases separation during the charge and discharge by contents of alkali ion in the lattice. This does not give rise to general structural variations but affect electrochemical performances and reportedly known to be related to the particle size [8-10]. For example, it is well known that electrode materials such as $LiFePO_4$ has two binary phase Li_aFePO4 and $Li_{1-b}FePO_4$

whose solid solubility limits, a and b. The solid-solid phase transitions are first order and the enthalpy change can be described as follows [11]:

$$\Delta H = \Delta H_{\text{intrinsic}} + \Delta H_{\text{particle}} \qquad (3.14)$$

Therefore, if particle size decreases, Gibbs free energy of mixing (ΔG_{mix}) would be reduced by the contribution of penalty in elastic energy at two phase boundary. This means that miscibility gap between two phases has been reduced along with extension of solid-solution charge and discharge curves, which is indicative of better diffusion and lower mismatch along two phase boundary when particle size is reduced. In this context, attempts to improve the electrochemical properties of $LiTi_2(PO_4)_3$ by nano-sizing [12] and controlling the oxygen vacancy [13] have previously been reported. Meanwhile, the use of Li-rich lithium titanium phosphate phases instead of current $LiTi_2(PO_4)_3$ has not been described yet. We considered that the use of Li-rich phases of $Li_{1+x}Ti_2(PO_4)_3$ could be expected to improve the cycle life at the expense of somewhat lowered capacity until suppliable lithium in the lattice structure is completely depleted according to following mechanism:

During Li^+ insertion:

$$Li_{1+x}Ti_2(PO_4)_3 + (2\text{-}x)Li^+ + (2\text{-}x)e^- \rightarrow (1\text{-}z)Li_3Ti_2(PO_4)_3 +$$

$$z[Li_{3\text{-}0.5y}Ti_2(PO_4)_3/Li_{3+0.5y}Ti_2(PO_4)_3]\ ;\ z \sim 0 \qquad (3.15)$$

During Li^+ extraction:

$$(1\text{-}z)Li_3Ti_2(PO_4)_3 + (0.5z)Li_{3\text{-}0.5y}Ti_2(PO_4)_3 \rightarrow Li_{1+x\text{-}0.5y}Ti_2(PO_4)_3 + (2\text{-}x)Li^+ + (2\text{-}x)e^- \qquad (3.16)$$

Interestingly, Li-rich phase, $Li_{1+x}Ti_2(PO_4)_3$, has been known as orthorhombic superionic phase which exists in a space group system different from that of $LiTi_2(PO_4)_3$ (*R-3c*). This observation suggests that initially preparable orthorhombic phase could be categorized as completely different material from that prepared by electrochemical means. On the other hand, our preliminary attempts to synthesize Li-rich single-phases of $Li_{1+x}Ti_2(PO_4)_3$ ($0 \leq x \leq 2$) revealed that this Li-rich phase could easily be incorporated with the well-known rhombohedral $LiTi_2(PO_4)_3$ contaminated with some other stable phases in the compositional space Li-Ti-P-O, such as $LiTiPO_5$, $Li_4Ti_5O_{12}$, $LiTi_2(PO_4)_3$, and TiO_2, depending on the synthesis temperature and the stoichiometry of the starting materials [14]. A systematic approach to stabilize isotypic mixed-valent structures was previously pioneered by M. Catti. In that work, it was suggested that mixed-valent superstructures of $Li_{1+x}In_xTi_{2\text{-}x}(PO_4)_3$ could exist when $x < 0.5$ or $x > 1.0$ [15], which is

in good agreement with our preliminary data and previously reported data (**Table 3-2**). Therefore, the smallest amount of lithium, x=1.5, was chosen to isolate the single phase of mixed-valent orthorhombic $Li_{1.5}Ti_2(PO_4)_3$.

In this preliminary study, we tried to clarify how electrochemical properties could vary in the seemingly similar compounds $LiTi_2(PO_4)_3$ and $Li_{1.5}Ti_2(PO_4)_3$. The electrochemical properties of these materials were evaluated versus Li metal to measure Li-ionic diffusivity of these structures. In addition, their feasibilities as anodes for aqueous lithium-ion cells were tested in $LiFePO_4//Li_xTi_2(PO_4)_3$ full-cell configurations using 1M Li_2SO_4 electrolytes.

Table 3-2. Reported structures of $Li_xTi_2(PO_4)_3$ and related $Li_x(TiM)_2(PO_4)_3$ phases on ICSD.

Type	Space group	ICSD #
$Li_{3.18}Ti_2(PO_4)_3$	*R-3*	95980
$Li_{2.72}Ti_2(PO_4)_3$	*Pbcn*	71277
$Li_{2.64}Sc_{1.8}Ti_{0.2}(PO_4)_3$	*Pbcn*	50422
$Li_2Ti_2(PO_4)_3$	*Pbcn*	261825
$Li_2Ti_{0.925}Fe_{1.075}(PO_4)_3$	*Pbca*	51332
$Li_{1.08}Ti_{1.4}Zr_{0.6}(PO_4)_3$	*R-3c*	166882
$LiTi_2(PO_4)_3$	*R-3c*	95979
$LiTi_{0.2}Sn_{1.8}(PO_4)_3$	*R-3c*	183678
$Li_{0.9}Ti_{1.8}Nb_{0.2}(PO_4)_3$	*R-3c*	184087

3.2. Experimental

Rhombohedral $LiTi_2(PO_4)_3$ (RLTP) and orthorhombic $Li_{1.5}Ti_2(PO_4)_3$ (OLTP) were synthesized via sol-gel synthesis. A stoichiometric combination of the starting materials, $LiOH{\cdot}H_2O$ (Sigma-Aldrich), $Ti[OCH(CH_3)_2]_4$ (Sigma-Aldrich), $NH_4H_2PO_4$ (Nacalai Tesque), and citric acid (10% by weight) was dissolved in 100 mL water and stirred at 80 °C for 12 h. The mixture was pre-heated at 300 °C for 5 h, and then further sintered at 700 °C for 12 h under Ar flow. Commercial $LiFePO_4$ (Hohsen Corp.) was used as the cathode in full-cells.

X-ray diffraction patterns of the as-synthesized materials were obtained by an X-ray diffractometer (XRD, Rigaku; Cu-Kα, 50 kV, 300 mA) in 2Θ range of 10-80° at a scan rate of 0.1°/min with a step size of 0.02° and refined by the Fullprof Suite refinement program. The atomic coordinates and atomic displacement parameters for OLTP were obtained from previously reported $Li_2Ti_2(PO_4)_3$ single crystal data [16] and used for further refinement. The background of the XRD profile was fitted with linear interpolation between a set of 55 points with refinable heights, and the peak shape was refined with the convolution of a pseudo-Voigt function.

The electrical conductivity of the samples was evaluated using a powder resistivity measuring system (Mitsubishi Chemical Analytech). The resistivity measuring system is equipped with a high precision pressure gauge directly attached to a Teflon-coated cylindrical holder (model MCP-PD522), allowing measurements under various

pressures while accounting for the thickness, volume, and density of the sample under that pressure.

The working electrodes were prepared by ball-milling a mixture of 70 wt.% electrode active materials and 25 wt.% acetylene black. Then, 5 wt.% PTFE binder was added to the mixture, and approximately 5 mg of pellets were prepared manually using a mortar and pestle. The electrode pellets were vacuum-dried at 100 °C overnight and then assembled in 2032 coin cells with 1 M $LiPF_6$ in EC:DMC (1:1 in volume). To balance the full aqueous cells, a comparably low current rate of 15 mA g^{-1} was applied for $LiFePO_4$, RLTP, and OLTP versus Li metal to obtain the initial specific capacities.

The cyclic voltammograms (CV) were measured in a range of scan rates to obtain the precise peak current, which was then treated by the Randles-Sevcik equation to estimate the Li^+ diffusion coefficient in both the OLTP and RLTP phases. To envisage the electrochemical performance of the full aqueous cells, the charge and discharge cycling were evaluated for $LiFePO_4$//$Li_xTi_2(PO_4)_3$ configurations with 1 M Li_2SO_4 electrolyte at 37.5 mA g^{-1} in the voltage range 0-1.2 V.

3.3. Results and Discussion

The XRD patterns of the as-synthesized RLTP and OLTP are illustrated in **Fig. 3-1**. The obtained XRD pattern for OLTP is well-matched with the simulated XRD powder pattern from OLTP single crystal data (ICSD #261825), with a slight shift to a higher

angle. RLTP with the space group of *R-3c* (#167) and OLTP with the space group of *Pbcn* (#60) [16, 17] have the same $M_2(PO_4)_3$ frameworks as the previously reported $Li_{3-x}M_2(PO_4)_3$ phases [15, 18], which consist of tetrahedral PO_4 linked together with four octahedral MO_6 to make infinite channels for Li ions to reside in.

Although these two building blocks are alternatively connected to produce nestlike frameworks for both structures, the stacking modes of $Ti_2(PO_4)_3$ are quite different between OLTP and RLTP, as illustrated in **Fig. 3-2**. The calculated atomic coordinates and equivalent symmetry codes used in **Fig. 3-2** are listed in **Table 3-3**. To determine the isotropic displacement parameters of refined atoms, the atomic coordinates were fixed before the final cycle of refinement and then released to assure the fitness of the refined atomic vibrations in the lattice, which resulted in unexpectedly higher deviations in the atomic coordinates of OLTP compared to those of RLTP. This result suggests that the 3-D channels in the OLTP framework may vary with the size of the octahedra and tetrahedra blocks, which are mainly determined by the valence of the central transition metal [19].

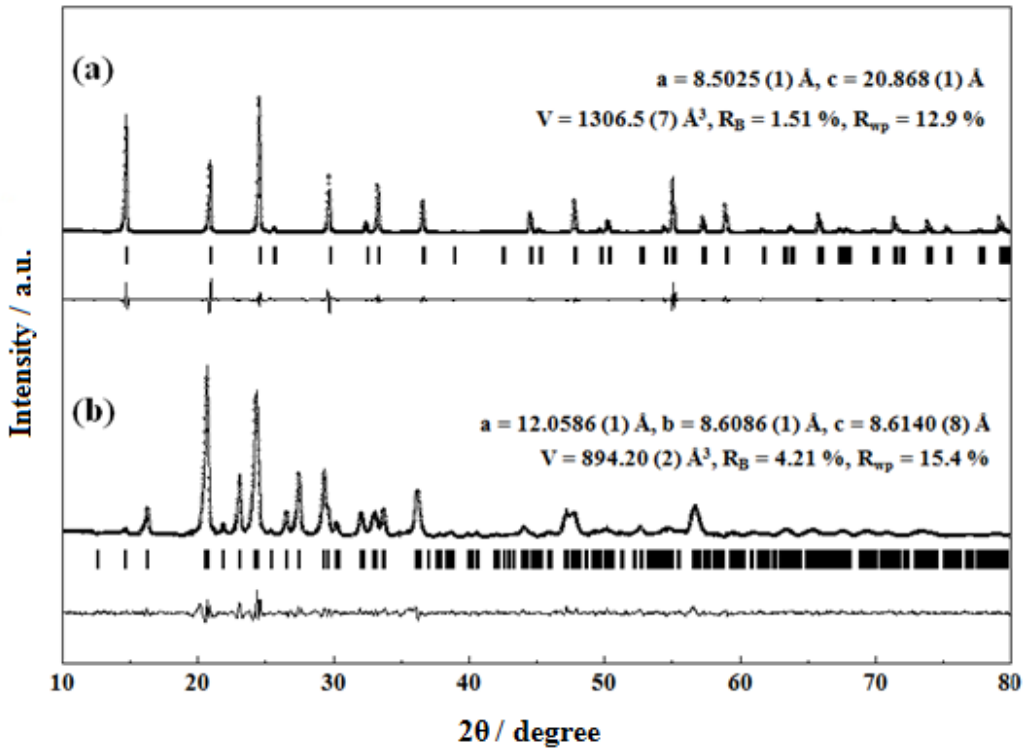

Fig. 3-1 Powder diffraction patterns of rhombohedral $LiTi_2(PO_4)_3$ (a) and orthorhombic $Li_{1.5}Ti_2(PO_4)_3$ (b).

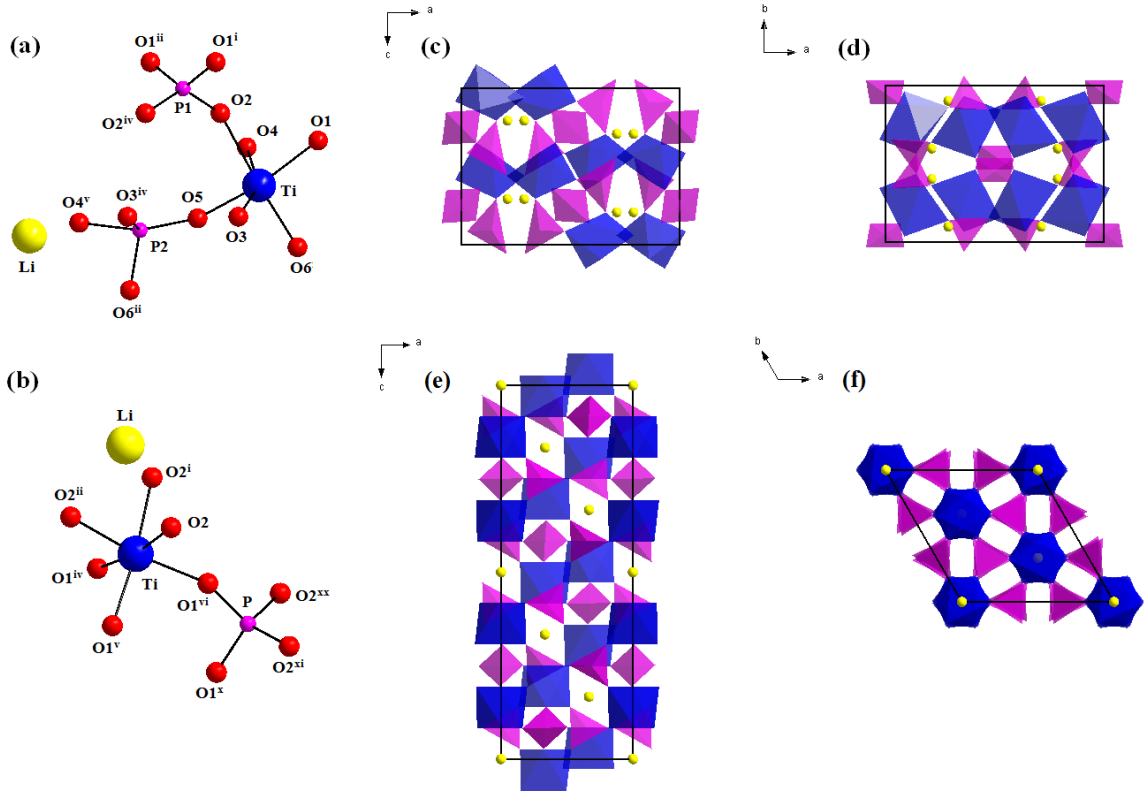

Fig. 3-2 Local coordination environments of the Ti and P atoms with the atom labeling scheme and the schematic views for orthorhombic $Li_{1.5}Ti_2(PO_4)_3$ (a, c, d) and rhombohedral $LiTi_2(PO_4)_3$ (b, e, f) along the b- and c-axes. Blue octahedra and purple tetrahedra represent TiO_6 and PO_4, respectively.

Table 3-3. Obtained atomic coordinates for rhombohedral $LiTi_2(PO_4)_3$ (a) and orthorhombic $Li_{1.5}Ti_2(PO_4)_3$ (b). The symmetry codes illustrated in Fig. 3-2 are as follows: (i) -x+y, -x, z, (ii) -y, x-y, z, (iv) -1-x+y, -x, z, (v) 1-y, 1+x-y, z, (vi) x, -1+y, z, (x) 1+x-y, 1-y, 1/2-z, (xi) 2/3-x, 1/3-y, 1/3-z, (xx) 1/3-x+y, -1/3+y, 1/6+z for rhombohedral $LiTi_2(PO_4)_3$ and (i) 1-x, 1-y, -z, (ii) x, 1-y, 1/2+z, (iv) 1-x, y, 0.5-z, (v) 1/2-x, 1/2-y, 1/2+z for orthorhombic $Li_{1.5}Ti_2(PO_4)_3$.

(a)	*x*	*y*	*z*	**(b)**	*x*	*y*	*z*
Li	0.00000	0.00000	0.00000	Li	0.342(1)	0.113(2)	0.761(1)
Ti	0.00000	0.00000	0.1428(1)	Ti	0.3902(6)	0.2461(2)	0.0291(6)
P	0.2951(6)	0.00000	0.25000	P1	0.50000	0.526(4)	0.25000
O1	0.1897(2)	0.9903(3)	0.1935(9)	P2	0.3433(2)	0.107(2)	0.381(2)
O2	0.1821(2)	0.1628(2)	0.0817(5)	O1	0.4295(2)	0.385(4)	0.860(4)
				O2	0.4081(2)	0.462(3)	0.129(3)
				O3	0.534(2)	0.158(4)	0.064(3)
				O4	0.219(2)	0.328(4)	0.032(3)
				O5	0.318(3)	0.156(3)	0.225(4)
				O6	0.352(4)	0.063(4)	0.938(4)

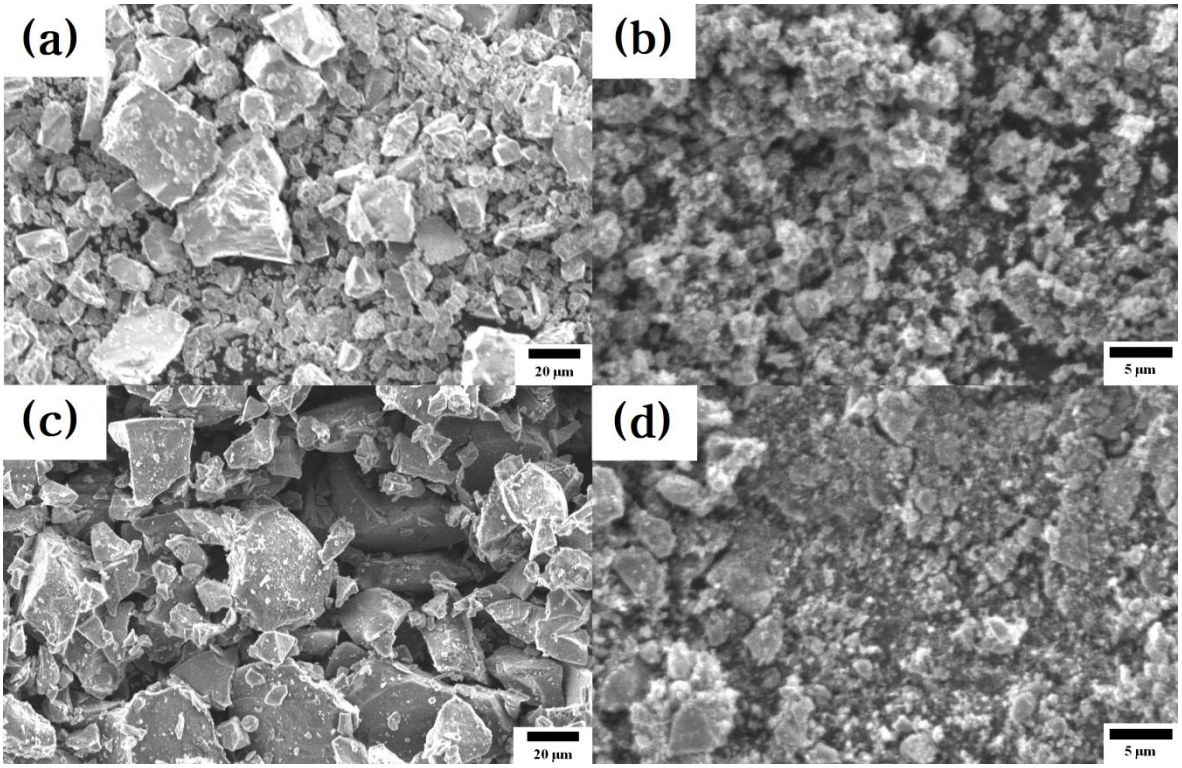

Fig. 3-3 SEM images of rhombohedral $LiTi_2(PO_4)_3$ (a), rhombohedral $LiTi_2(PO_4)_3$/C (b), orthorhombic $Li_{1.5}Ti_2(PO_4)_3$ (c), and orthorhombic $Li_{1.5}Ti_2(PO_4)_3$/C (d).

On the other hand, the framework of the RLTP lattice does not undergo such variation, which is in good agreement with the flat charge and discharge plateaus and two phase reaction mechanism. Some of the obtained crystals had optical sizes comparable to those of previously reported single crystals [16], as shown in **Fig. 3-3**. This indicates that the synthesis procedure and the stoichiometry of the starting materials in this work represent thermodynamically suitable conditions for isolating both title compounds, OLTP and RLTP. To investigate the fundamental electrochemical properties of the prepared electrode materials, the voltage windows of 3.0 – 1.5 V for RLTP and OLTP were applied and measured versus Li metal at a comparably low current rate of 15 mA g^{-1} as illustrated in **Fig. 3-4**. The obtained initial specific capacities of 122 mAh g^{-1} for RLTP, 101 mAh g^{-1} for OLTP, and 130 mAh g^{-1} for $LiFePO_4$ were then used to balance the full aqueous cells. Although rhombohedral and orthorhombic lithium titanium phosphates share the same framework with PO_4 and TiO_6 building blocks, the charge and discharge profiles of OLTP are different from those of RLTP. In fact, these smoothed charge/discharge profiles of OLTP are similar to those of the previously reported Zr-doped $Li_3V_2(PO_4)_3$ [20], which also shows smoothed solid-solution reaction properties and adopts the same standard space group of *Pbcn* (#60). To further understand OLTP and RLTP, Cyclic voltammograms (CV) of both materials were measured under various scan rates (0.0002 V s^{-1} – 0.00068 V s^{-1}) as illustrated in **Fig. 3-5**. The data were then treated by the Randles-Sevcik model [21, 22]:

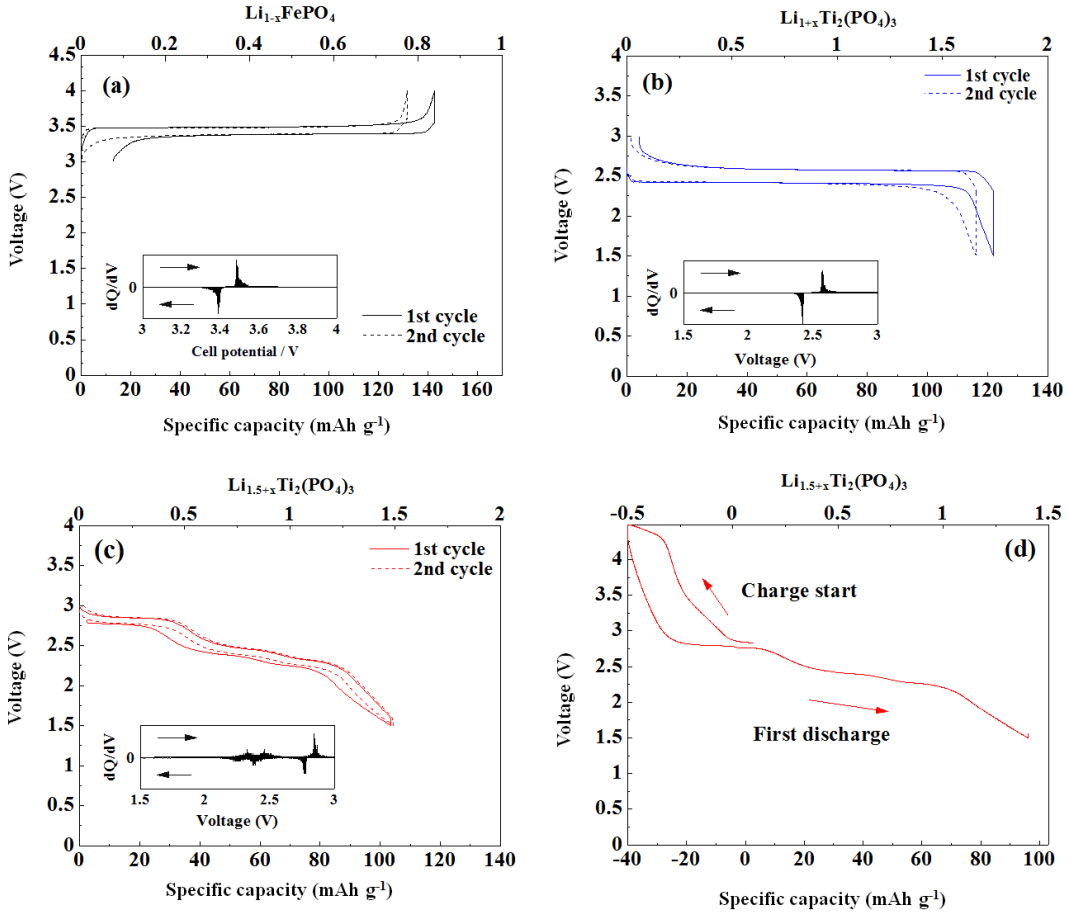

Fig. 3-4 Charge/discharge profiles of (a) $LiFePO_4$, (b) rhombohedral $LiTi_2(PO_4)_3$//Li, (c) orthorhombic $Li_{1.5}Ti_2(PO_4)_3$//Li from discharge start and (c) orthorhombic $Li_{1.5}Ti_2(PO_4)_3$//Li from charge start at a current rate of 15 mA g^{-1}.

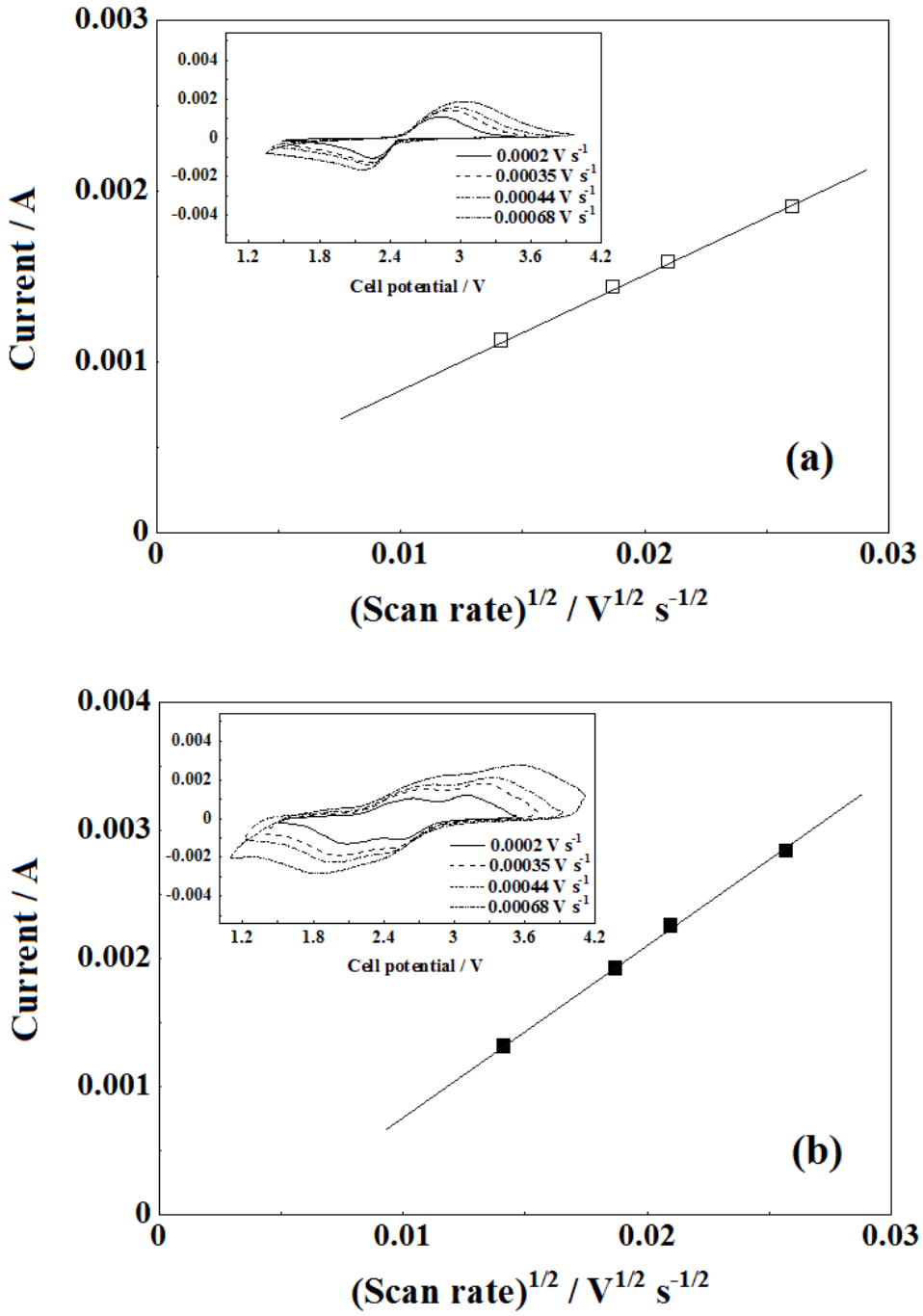

Fig. 3-5 CV Randles plots for rhombohedral $LiTi_2(PO_4)_3$ (a) and orthorhombic $Li_{1.5}Ti_2(PO_4)_3$ (b). The corresponding cyclic voltammograms are shown in the inset.

$$i_p = 0.4463\, nFAC(\, nFvD/RT\,)^{0.5} \qquad (3.17)$$

where 0.4463 is Randles-Sevcik constant, n is the number of electrons, F is the Faraday constant (96500 C mol^{-1}), A is the electrode surface area (cm^2) [23], C is the concentration of the electroactive species (mol cm^{-3}), v is the scan rate (V s^{-1}), and D is the diffusion coefficient (cm^2 s^{-1}).

The obtained diffusion coefficient (D) for RLTP was 5.94×10^{-15} cm^2 s^{-1}, which is fairly close to previously reported value [12]. On the other hand, slightly higher diffusion coefficient (D) of 1.05×10^{-14} cm^2 s^{-1} was obtained for OLTP. Since the electrochemical performance of the intercalation hosts depends on both the diffusion coefficient of Li^+ and the electrical conductivity of the host structure, the electrical conductivities of OLTP and RLTP were also measured by means of a powder resistivity system (Hiresta-UP). Although the obtained electrical conductivities of OLTP and RLTP are close to other NASICON-type host materials [24-26], it was found that the electrical conductivity of OLTP (1.036×10^{-5} S cm^{-1}) is an order of magnitude higher than that of RLTP (1.669×10^{-6} S cm^{-1}) in this study. Therefore, OLTP could be a good alternative for the RLTP anode as it has a slightly higher electrical conductivity and diffusion coefficient. To further investigate its feasibility as an anode in the full Li-ion aqueous cell configuration, electrochemical cycling tests versus $LiFePO_4$ as a cathode material

were performed using aqueous electrolyte (1 M Li_2SO_4) in the voltage range between 0 – 1.2 V at a current rate of 37.5 mA g^{-1}, as illustrated in **Fig. 3-6**. The use of RLTP or OLTP as an anode in full-cell configurations resulted in only a small difference in the initial discharge capacities of 100.2 mAh g^{-1} for $LiFePO_4$//RLTP and 103.8 mAh g^{-1} for $LiFePO_4$//OLTP at 37.5 mA g^{-1}. However, these differences became larger as the number of cycles increased: the capacities were 54 mAh g^{-1} for $LiFePO_4$//RLTP and 80 mAh g^{-1} for $LiFePO_4$//OLTP after 50 cycles. This result reveals that OLTP could be an attractive alternative for RLTP when the cycle performance of the anode material is the primary issue.

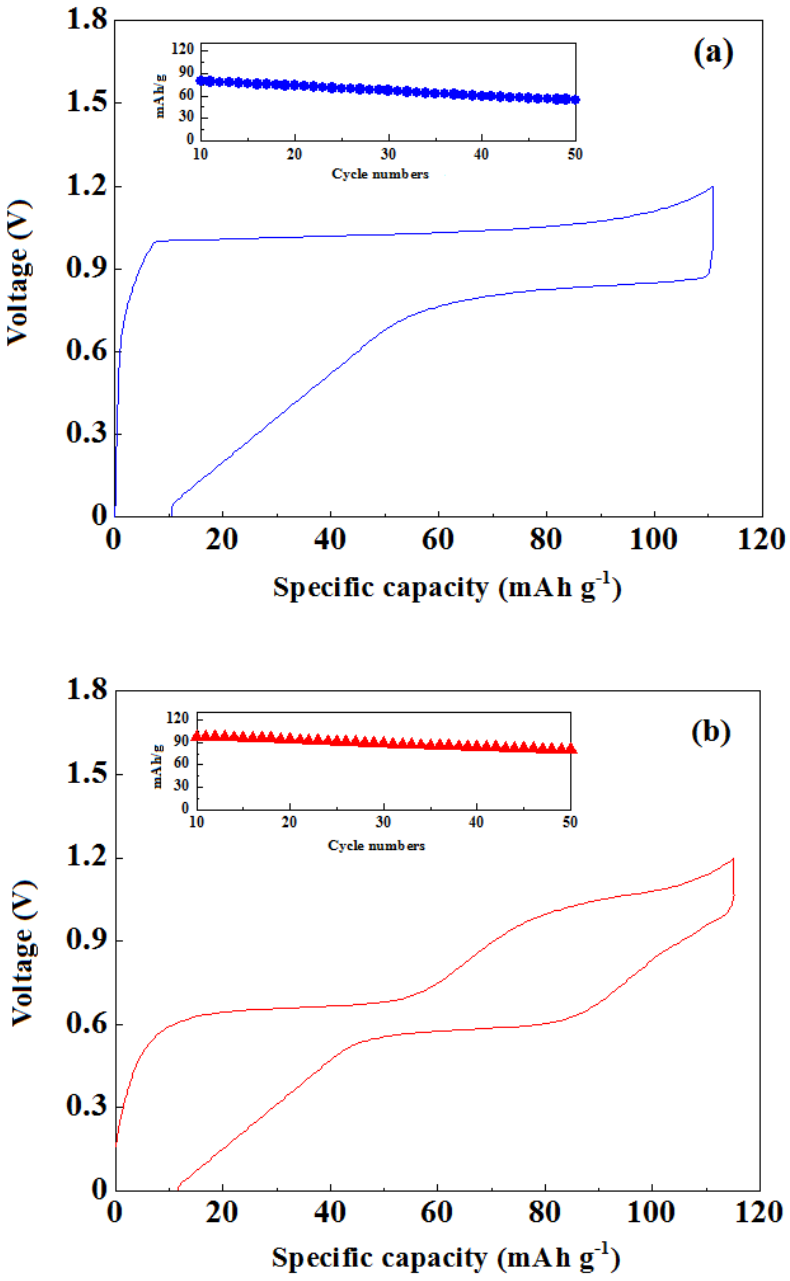

Fig. 3-6 Initial charge/discharge profiles and cycle abilities of $LiFePO_4$//rhombohedral $LiTi_2(PO_4)_3$ (a) and $LiFePO_4$//orthorhombic $Li_{1.5}Ti_2(PO_4)_3$ (b) full aqueous cells in the voltage range between 0 and 1.2 V at a current rate of 37.5 mA g^{-1}. The specific capacities of the full-cells were recorded based on cathode weight.

References

[1] M. B. Pinson and M. Z. Bazant, Cornell University Library arXiv:1210.3672 (2012).

[2] P. Liu, J. Wang, J. Hicks-Garner, E. Sherman, S. Soukiazian, M. Verbrugge, H. Tataria, J. Musser, and P. Finamore, *J. Electrochem. Soc.*, **157** (2010) A499.

[3] R. Ruffo, C.Wessells, R. Huggins, and Y. Cui, *Electrochem. Comm.*, **11** (2009) 247.

[4] Y. Cui, Y. Hao, W. Bao, Y. Shi, Q. Zuang, and Y. Qiang, *J. Electrochem. Soc.*, **160** (2013) A53.

[5] X. Liu, T. Saito, T. Doi, S. Okada, and J. Yamaki, *J. Power Sources*, **189** (2009) 706.

[6] L. Liu, F. Tian, X. Wang, and M. Zhou, *Acta Phys. -Chim. Sin*, **27** (2011) 2600.

[7] M. Vujkovi´ca, I. Stojkovi´ca, N. Cvjeti´canina, and S. Mentus, *Electrochim. Acta*, **92** (2013) 248.

[8] N. Meethong, H. -Y. S. Huang, W. C. Carter, and Y. -M. Chiang, *Electrochem. Solid-State Lett.*, **10** (2007) A134.

[9] G. Kobayashi, S. Nishimura, M. -S. Park, R. Kanno, M. Yashima, T. Ida, and A. Yamada, *Adv. Funct. Mater.*, **19** (2009) 395.

[10] N. Meethong, H. -Y. S. Huang, S. A. Speakman, W. C. Carter, and Y. -M. Chiang, *Adv. Funct. Mater.*, **17** (2007) 1115.

[11] R. Yazami, Nanomaterials for Lithium-Ion Batteries. Ed. by R. Yazami. Pan Stanford, 2014.

[12] H. Roh, H. Kim, K. Roh, and K. Kim, *RCS Adv.*, **4** (2014) 31672.

[13] J. Luo, L. Chen, Y. Zhao, P. He, and Y. Xia, *J. Power Sources*, **194** (2009) 1075.

[14] N. V. Kosova, D. I. Osintsev, N. F. Uvarov, and E. T. Devyatkina, *Chemistry for Sustainable Development*, **13** (2005) 253.

[15] M. Catti, *J. Solid State Chem.*, **156** (2001) 305.

[16] Y. Kee, S. Lee, and H. Yun. *Acta Cryst., E***67** (2011) i49.

[17] S. Wang and S. –J. Hwu, *J. Solid State Chem.*, **90** (1991) 377.

[18] S. Patoux, C. Wurm, M. Morcrette, G. Rousse, and C. Masquelier, *J. Power Sources*, **119** (2003) 278.

[19] B. Wang and M. Greenblatt, *Chem. Mater.*, **5** (1993) 23.

[20] M. Sato, H. Ohkawa, K. Yoshida, M. Saito, K. Uematsu, and K. Toda, *Solid State Ionics*, **135** (2000) 137.

[21] P. Zanello. "Inorganic Electrochemistry" Theory, Practice and Application, 978-0-85404-661-4, The Royal Society of Chemistry, 2003.

[22] A. J. Bard and L. R. Faulkner. Electrochemical Methods: Fundamentals and Application, *2*nd Ed. 978-0-471-04372-0, WILEY, 2000.

[23] J. Wolfenstine, J. L. Allen, and J. Sumner. Tech. rep. Adelphi, MD 20783-1197: Army Research Laboratory, 2009.

[24] Y. Kee, N. Dimov, E. Kobayashi, A. Kitajou, and S. Okada, *Solid State Ionics*, **272** (2015) 138.

[25] Z. Chen, H. Jin, C. Dai, G. Wu, M. Nelson, and Y. Cheng, *Int. J. Electrochem.*

Sci. ,**8** (2013) 8153.

[26] A. C. M. Rodrigues and J. L. Narvaez-Semanate, *Solid State Ionics*, **181** (2010) 1197.

CHAPTER 4

Conclusions

In this study, NASICON-type host material $Li_3V_2(PO_4)_3$ and its Al- and Fe-doped derivatives were synthesized and incorporation of the dopants in the parent crystal structure was confirmed by powder X-ray diffraction. Single phase orthorhombic $Li_{1.5}Ti_2(PO_4)_3$ with structure completely different from the commonly known rhombohedral $LiTi_2(PO_4)_3$ was also isolated. These compounds were studied as Li^+ hosts.

$Li_3V_2(PO_4)_3$ and its Al- and Fe-doped derivatives $Li_3V_{1.9}M_{0.1}(PO_4)_3$, were synthesized via a spray-drying assisted carbothermal reaction. All samples are impurity-free monoclinic phases owing to the spray-drying-assisted carbothermal synthetic route. $Li_3V_2(PO_4)_3$ and its doped derivatives were tested in symmetric cells with either liquid electrolyte, 1 M $LiPF_6$ in EC:DMC (1:1 in volume), or solid-state electrolyte, $Li_{1.5}Al_{0.5}Ge_{1.5}(PO_4)_3$, respectively. All-solid-state symmetric cells $Li_3V_{1.9}M_{0.1}(PO_4)_3$/ $Li_{1.5}Al_{0.5}Ge_{1.5}(PO_4)_3$/$Li_3V_{1.9}M_{0.1}(PO_4)_3$ show larger capacity due to Fe and Al doping. First discharge capacities of the Al- and Fe-doped samples were 107.6 mAh g^{-1} and 105.6 mAh g^{-1} in the voltage range 0-3.0 V at a current rate of 7.5 mA g^{-1}, in comparison with the first discharge capacity of 103.3 mAh g^{-1} for $Li_3V_2(PO_4)_3$. Therefore, the feasibility of all-solid state symmetric cells using either pure or doped $Li_3V_2(PO_4)_3$ samples was confirmed. Improved electrochemical performance could be attributed to:

1. Greater electrical conductivity of the doped $Li_3V_{1.9}M_{0.1}(PO_4)_3$ materials compared with the undoped $Li_3V_2(PO_4)_3$

2. Enhanced particle crystallization when isovalent Al^{3+} and Fe^{3+} are introduced into vanadium sites with the same symmetry $P2_1/c$

3. Reduced particle size of doped $Li_3V_{1.9}M_{0.1}(PO_4)_3$ materials compared with that of the undoped $Li_3V_2(PO_4)_3$

Here, the relationship between electrical conductivity and doping is not straightforward. However, the increased electrical conductivity and improved cyclic performance could be attributable to better crystal integrity and reduced lattice strain during charge/discharge [1, 2].

On the other hand, we expect that better rate performance, longer cycle life and lowered polarization in all-solid-state symmetric cells could be met if the interfacial resistance within the all-solid-state symmetric cells could be further reduced. In our study the all-solid-state cells still show huge polarization and continuous capacity fade upon cycling. As mentioned in the previous section, this should be attributed to complicated charge transfer resistance mechanism originating from:

1. Electrode-electrolyte boundary

2. Intergrain resistance

To mitigate this huge resistance, better preparation of electrode-electrolyte interphase is necessary, which could not be achieved by conventional hot-pressing process. This preparation method may include Pulsed Laser Deposition (PLD), which is suitable for the growth of thin-layers from vaporization of the target material. The second possible way of mitigating this issue may also come from the use of superionic orthorhombic phases, which could be induced by doping aliovalent atoms such as Zr. Although doping of this electrochemically inactive atom would decrease the theoretical capacity of the pristine $Li_3V_2(PO_4)_3$, additional increase of electrical conductivity and ion diffusivity may be achieved which was confirmed by investigating the orthorhombic $Li_{1.5}Ti_2(PO_4)_3$, which results in improved electrochemical performance even without the need of complicated optimization steps such as particle downsizing, including more conductive additives, etc.

RLTP and OLTP were synthesized via the sol-gel method and examined as anode materials for rechargeable Li-ion batteries. The resistivity measurements and CV results indicated that OLTP has a higher Li^+ diffusivity and higher electrical conductivity than RLTP. In addition, the feasibility of OLTP as an alternative to the well-known RLTP anode material was further investigated by using $LiFePO_4$//OLTP full aqueous cells, which showed greater cyclic performance than $LiFePO_4$//RLTP full aqueous cells in the voltage range between 0 and 1.2 V. This preliminary research reveals that OLTP could

be an attractive alternative for RLTP when the cycle performance of the anode material is the primary issue. On the other hand, the enhanced electrochemical properties of orthorhombic $Li_{1.5}Ti_2(PO_4)_3$ is somewhat interesting because this compound has seemingly the same empirical formula with previously well-known rhombohedral $LiTi_2(PO_4)_3$ but shows completely different electrochemical performance (e.g. solid-solution reaction). Although the charged states of both OLTP and RLTP are represented by the same empirical formula $Li_3Ti_2(PO_4)_3$, their band structures seem different. For example, optical color of pure RLTP is white while that of OLTP is grey which is in a good agreement with slightly increased electrical conductivity of OLTP [3]. The increased diffusivity of OLTP could be attributable to short Li-Li distance and comparably high isotropic displacement parameter of Li (~0.1 $Å^2$) compared to that of RLTP (~0.05 $Å^2$).

However, in our study we could not obtain stable enough cyclic performance in the aqueous full-cell configurations. Poor cycling performance of aqueous full-cells at low current density has been discussed many times in the literature, but it is not very clearly understood yet. The most probable reason for unsatisfactory cycle life performance is the presence of oxygen in the water. The voltage of Li-O_2 reaction equilibrium is a function of *pH*:

$$V = 4.268 – 0.059pH \qquad (4.1)$$

According to eq. 4.1, at potential below 3.85 V (vs. Li/Li^+), the anode immersed in the aqueous electrolyte becomes unstable and Li^+ might be leached to the electrolyte, which causes gradual capacity loss [4, 5]. For the case of RLTP and OLTP, the possible net Li leaching reaction may be expressed by the following equation:

$$Li_3Ti_2(PO_4)_3 + 0.25O_2 + 0.5H_2O \rightarrow LiOH + Li_2Ti_2(OH)(PO_4)_3 \qquad (4.2)$$

The phase $Li_2Ti_2(OH)(PO_4)_3$ may further decompose to other products. Regardless of the structure of the compound, main characteristic of the oxidation process is generation of LiOH and converting the active lithium titanium phosphate into inactive hydroxoposphate with possible further transformations. In this context, removing oxygen from the solution (heating, Ar-bubbling, using oxygen scavenger, etc.) should be an efficient technique to enhance the cycle performance of the aqueous full-cells.

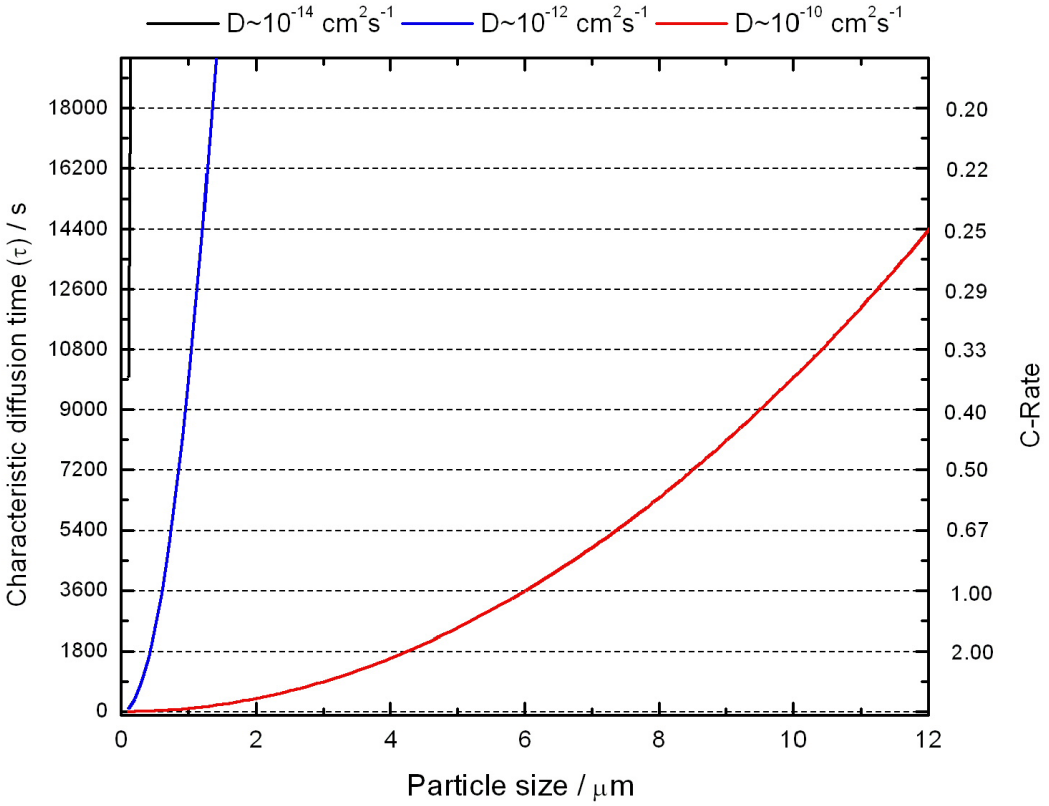

Fig. 4-1 Characteristic diffusion time [s] (left) and the corresponding C-rate (right) vs. particle size. Three different values of *D* are considered: 10^{-14} (black), 10^{-12} (blue) and 10^{-10} (red) $cm^2\ s^{-1}$.

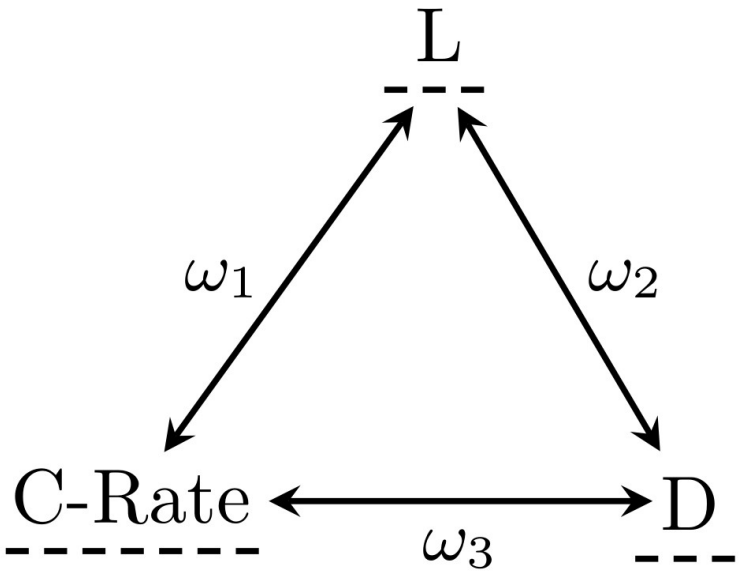

Fig. 4-2 Triangle diagram schematically showing the relationship between the Diffusion coefficient (*D*), mean particle size (*L*) and theoretical C-Rate of the electrode prepared with active material with diffusion coefficient *D* and mean particle size distribution *L*.

Diffusivity of the charge carriers (in this case Li^+) within the solid-state phase is another important feature of any candidate battery material, based on the intercalation principle of operation. Diffusivity is characterized quantitatively by the diffusion coefficient *D* [$cm^2 s^{-1}$]. The diffusion coefficient is typically used as a scaling factor in the Fick's laws. In the context of the battery materials, a key relationship between the mean particle size, and characteristic diffusion time is given by the following relationship:

$$\tau = \frac{L^2}{D} \qquad (4.3)$$

where *L* is the migration distance for Li^+ [cm] and *D* is the diffusion coefficient [$cm^2 s^{-1}$]. A simulation showing characteristic diffusion time vs. particle size is shown in **Fig. 4-1**.

It allows us to answer basic questions regarding the suitability of a particular Li^+ host as a battery material. If we know *D* it is possible predict the required particle size necessary to achieve certain C-rate performance. Conversely, one could estimate the necessary *D* if particle size of the electrode active material should be above certain limit. Decreasing particle size could, in principle increase the rate performance even for materials with sluggish kinetics. This is why there are many recent works suggesting the

use of cathode nanomaterials. However, nanometarials have low TAP density. In addition, their huge specific surface area causes severe side reactions. Use of nanomaterials also leads to safety concerns. Therefore in the technically interesting cases battery manufacturers are willing to use materials with particle size around several micrometers. The relationship between particle size, *D*, and C-rate performance is schematically shown in **Fig. 4-2**. In this study, we could successfully optimize homogenous particle size distribution by spray-drying process, which allows us to consider diffusion coefficient (*D*) and mean particle size (*L*) in terms of rate performance for the future study. From the above discussions, we could conclude the possible applications of NASICON-type materials for energy storage systems as follows:

1. Generally low diffusion coefficients of (anti)-NASICON-type materials could be enhanced by doping isovalent ion in metal sites (M) along with enhancement in electrical conductivity.

2. Generally low diffusion coefficients of (anti)-NASICON-type materials could be enhanced by doping aliovalent ion in the metal sites (M) with phase transformation to orthorhombic.

3. To use general (anti)-NASICON-type materials for high power applications, the use of homogeneous and sub-micrometer-sized particles are necessary.

References

[1] A. S. Wochnik, M. Handloser, D. Durach, A. Hartschuh, and C. Scheu, *ACS Appl. Mater. Interfaces*, **5** (2013) 5696.

[2] M. Ren, Z. Zhou, Y. Li, X. P. Gao, and J. Yan, *J. Power Sources*, **162** (2006) 1357.

[3] Y. Kee, S. Lee, and H. Yun, *Acta Cryst*., *E***67** (2011) i49.

[4] Y. Wang, J. Yi, and Y. Xia, *Adv. Energy Mater*., **2** (2012) 830.

[5] Y. Xia, W. –J. Cui, P. He, and Y. –Y. Xia, *Nat. Chem.*, **2** (2010) 760.